View metadata, citation and similar papers at core.ac.uk

brought to you by CORE

provided by Illinois Digital Environment for Access to Learning and Scholarship Repository

© 2012 Loan Thi Kieu Vo

PREDICTING LEARNING SUCCESS FROM PATTERNS OF PRE-TRAINING MAGNETIC RESONANCE IMAGES

BY

LOAN THI KIEU VO

DISSERTATION

Submitted in partial fulfillment of the requirements
for the degree of Doctor of Philosophy in Electrical and Computer Engineering
in the Graduate College of the
University of Illinois at Urbana-Champaign, 2012

Urbana, Illinois

Doctoral Committee:

Professor Zhi-Pei Liang, Chair
Associate Professor Michelle Y. Wang, Director of Research
Professor Narendra Ahuja
Adjunct Assistant Professor Todd Coleman
Professor Arthur F. Kramer
Assistant Professor Dirk B. Walther, The Ohio State University

ABSTRACT

Performance in most complex cognitive and psychomotor tasks improves with training, yet the extent of improvement varies among individuals. Is it possible to forecast the benefit that a person might reap from training? What is the mechanism underlying learning? Several behavioral measures have been used to predict individual differences in task improvement, but their predictive power is limited. Our multi-voxel pattern analysis (support vector regression) of the time-averaged blood oxygen level dependent (BOLD) brain activity in the dorsal but not the ventral striatum, recorded *before* training, predicts subsequent learning success with high accuracy. The fact that the high prediction accuracy of the data did not depend on the task subjects were performing during the recording might suggest that individual differences in neuroanatomy or persistent physiology predict whether and to what extent people will benefit from training in a complex task.

To find out the physiology behind the possibility of predicting learning from time-averaged T2*-weighted images, a follow-up experiment was designed and performed with additional magnetic resonance (MR) measurements, including susceptibility-sensitive ones, such as susceptibility-weighted imaging (SWI), T2-, T2*-quantitative as well as diffusion tensor imaging (DTI) and arterial spin labeling (ASL). We then discovered that (patterns of) nonheme iron (not heme) is the underlying factor driving learning prediction. This discovery of the relationship between iron concentrations and learning ability in healthy young adults could not only guide the development of potential neuromarkers for a person's memory and executive control functions, but also help design customized learning-interventions to improve cognition or prevent its decline.

Út kính tặng ba, má, các chị và anh

ACKNOWLEDGMENTS

First of all, I would like to express my highest appreciation to my research advisors, Dr. Dirk B. Walther, Dr. Michelle Y. Wang and Dr. Arthur F. Kramer. I am forever grateful to them for their wonderful and constant support. Receiving their brilliant advice and being given extraordinary working conditions, I owe my research accomplishments to them.

Furthermore, I might not have been able to go through these difficult times in my work and personal life at all, nor enjoy life as much as I do now, without their kind support and encouragement. My words are really far from being able to describe either their fantastic support or my heartfelt thanks to them. So thank you so very much again and again.

Next, I would like to express my sincere thanks to Dr. Zhi-Pei Liang for his guidance and support–especially in the early stages of my studying at UIUC. I really enjoyed listening to his views about many different things. I am very grateful to Dr. Liang, Dr. Narendra Ahuja and Dr. Todd P. Coleman, who serve as members on my thesis committee, for their constructive criticism and support.

I am also very thankful to Dr. Farzad Kamalabadi and Dr. Minh Do. They were so kind, so patient and so supportive. Without their encouragement and recommendations a few years ago, I could not have kept going in my program.

Besides these, I am obliged to all of the following people for their help and valuable discussions: Dr. Diego Hernando, Dr. Justin P. Haldar, Dr. Brad Sutton, Ouyang Cheng, Dr. Michelle W. Voss, Dr. Hyunkyu Lee, Dr. Ruchika S. Prakash, Dr. Kirk Erickson, Dr. Walter R. Boot, Dr. Gabriele Gratton, and the staffs and students of the Biomedical Imaging Center and the Lifelong Brain and Cognition Laboratory. It has

been a great pleasure and a true blessing to have had the opportunity to work with and learn from them.

Also, I would like to acknowledge the support of the Vietnam Education Foundation, especially its first president Mr. Kien Pham who has shown great leadership and innovation, and the Graduate College and the Department of Electrical and Computer Engineering at the University of Illinois at Urbana-Champaign for providing me the fellowship - the amazing chance to begin my journey here and all of the support throughout all my studying years. Additionally, I would like to acknowledge the research grants from the Office of Naval Research.

Actually, the journey would have been tougher and more lonesome if I had not been so lucky as to become friends with lots of wonderful people. Their sharing, helping hands, and laughter (and sometimes tears) made Urbana-Champaign for me not a corn-field with frost-bitten winter chill but a home away from home. Some of them indeed touched my life in a profound way. These friends are anh Tùng, Hoa, anh Lộc, chị Tú Anh, Justin, Tim, chị Lý, chị Phương, Thứ, anh Nam, chị Huyên, chị Tâm, the Norrises, anhNghĩa, chị Vân, Quang, em Nhung, em Vượng, em Đức Anh, anh Kiên, anh Duẫn, chị Nhàn, Diego, Oanh, em Quang, Nguyên, Zhu-bin, Dan, Cornelius, Nancy, Holly and Susie. Needless to say, I am also thankful for the love and care I have been receiving from my buddies in Vietnam including Châu, Minh, Tôn Nhân, Nhi, Phụng, and Liên.

Lastly but most importantly, I would like to thank my beloved family, including my parents, blood and in-law siblings, nephews and niece. For all the love and devotion, which many times has meant sacrifice, that have been given to me, I owe my everything to Ba, Má, chị Hai, anh Ba, chị Tư.

TABLE OF CONTENTS

LIST OF TABLES

LIST OF FIGURES

CHAPTER 1

INTRODUCTION

1.1 Problem formulation

People vary in their ability to improve cognitive and psychomotor performance with practice and training. Cognitive tests predict who will benefit from training [1, 2], but they usually account for only a small proportion of the variance among individuals [3]. Here we use brain magnetic resonance imaging (MRI) data to predict individual learning success with unprecedented accuracy. Specifically, from data collected in the original study in 2008, we showed that patterns of time-averaged T2*-weighted images in the dorsal striatum *at the start of training* for a complex video-game account for more than *half of the variance* in the amount of *subsequent learning* among individuals.

With a few exceptions (e.g., the volumetric study by Erickson et al. [4]), learning studies based on functional MRI (fMRI) typically make use of contrasts in the blood-oxygen-level dependent (BOLD) effect [5]. Measured with gradient-echo echo planar imaging (EPI), functional BOLD activity is obtained by contrasting the EPI images of an experimental condition of interest with those of a baseline condition. This emphasizes the differences between the two conditions and eliminates the common components in the BOLD signal. In this work, we focus on the common part, which we obtain by averaging the EPI volumes over time. The result is a time-averaged T2*-weighted image. Unlike T1- or T2-weighted images, which reflects the tissues' T1- or T2- contrasts, respectively, T2*-weighted images are sensitive to local field variations, which might be caused by local magnetic susceptibility difference between interested tissues and their surroundings [6, 7] – for

example, T2*-weighted has been used to measure iron deposited in the heart because (super-) paramagnetic iron substances creates local magnetic field inhomogeneity [8]. Using multi-voxel pattern analysis (MVPA) we identified patterns of time-averaged T2*-weighted activity that predict subjects' future improvements in playing a complex video game with high accuracy. Surprisingly, predictions from white matter were highly accurate, while voxels in the gray matter of the dorsal striatum did not contain any information about future training success. Prediction accuracy was higher in the anterior than the posterior half of the dorsal striatum.

More specially, all of these observations remained similar when we looked into data collected inside the magnet from different blocks during which subjects were doing different tasks. Nevertheless, the physical and physiological effects underlying this learning prediction power of the time-averaged T2*-weighted signal are so far unclear. Therefore we conducted a new study in which we designed the imaging sessions with many more sequences detecting susceptibility information as well as quantitatively measuring T2 and T2* values. We aimed to develop a comprehensive theory of the time-averaged T2*-weighted signal and its relation to cognitive performance based on a thorough analysis of the newly added scan sequences.

1.2 Overview of contributions

The ability to predict who will benefit from training by using neuroimaging data collected early in training may have far-reaching implications for the assessment of candidates for specific training programs, as well as for the study of populations that show deficiencies in learning new skills. In addition, the link between training ability and the time-averaged T2*-weighted signal in the dorsal striatum reaffirms the role of this part of the basal ganglia in learning and executive functions such as task switching and task coordination processes.

Furthermore, our non-invasive imaging studies on young healthy adults suggested the roles of nonheme brain iron (unrelated to hemoglobin, mostly in the form of

storage proteins, of which ferritin is the predominant form), and not heme iron (iron in hemoglobin), in performance improvement. As far as we know, ours is the first imaging study connecting brain iron pattern/distribution (in the striatum) and learning of each healthy individual. Previous proofs on both human and non-human models discuss only group differences in learning between iron-deficient and healthy controlled populations. Particularly, in a water-maze learning study of Yehuda et al. [9], rats that were fed an iron-free diet had significant learning deficits compared to the control group. These discrepancies happened even prior to drops in rats' hemoglobin levels yet remained after the hemoglobin level was reestablished. In another study on human young adults, non-anemic iron-deficient young adults with iron-supplement in 8 weeks showed better learning than the placebo group [10]. A good review (on both animal and human models) on effects of iron deficiency on learning and how this effect can possibly be explained at the neuronal cellular level can be found in [11].

Finally, our analysis used the patterns of time-averaged T2*-weighted images which are simply the time averaged of the popularly collected blood-oxygen-level-dependent BOLD signal, and thus the technique can be easily, and even retrospectively, applied to other studies.

1.3 Outline of the dissertation

This dissertation reports two studies related to learning prediction and the underlying mechanisms. The first study started in 2008 (it will be referred to as the 2008 study), and we included data from 34 young participants in our final analyses. The second study (called the 2010 study) was a follow-up study designed to discover answers for questions that remained from the first one, and in particular the mechanisms that led to the high levels of prediction of training effects; data sets from 39 young participants were included in our analyses.

In Chapter 2, the motivation of both the 2008 and 2010 studies will be discussed. We will examine scientists' desires to discover the mechanisms of learning, about

which, in spite of many research efforts, little is yet known.

In fact, there are many studies about learning based on humans, primates, and non-human animals. So far they have been pointing to the role of the striatum in learning. With that support from the literature, our study focuses only on that region. In Chapter 2, a detailed description of the striatum region will be provided.

As stated, the subjects in this study are human young adults; therefore, we can only perform a limited set of non-invasive measurements, including magnetic resonance imaging. However, learning is so complex that an analysis tool that fails to include individually specific information when extracting useful information would seem far from adequate in a study of the learning mechanism. Therefore, instead of voxel-based analysis, in our study we have applied a pattern analysis technique rooted in machine learning: support vector regression. It will be explained in Chapter 2 as well.

Furthermore, the last part of Chapter 2 will review MRI signal generation and data collection. These provide a foundation for understanding the connections between the different MR measurements in our studies and thus our conclusion about the possible source of the effect on learning.

In Chapter 3, we will present the results of learning-prediction from the 2008 study data. This research shows that individual differences in the patterns of time-averaged T2*-weighted MRI images of the dorsal striatum recorded in the initial stage of training predict, with high accuracy, subsequent learning success in a complex video game. These predictions explained more than half of the variance in the learning success of the individuals, suggesting that individual differences in neuroanatomy or persistent physiology predict whether and to what extent people will benefit from training in a complex task.

Nevertheless, experimental data in the 2008 study could not show precisely which intrinsic properties of the brain tissues or neuronal connections/organization within the dorsal striatum underlie the high accuracy of prediction. To reveal underlying mechanisms, we conducted a new MRI experiment in 2010 with a variety of imaging contrasts to look separately at different aspects of the brain structure/components to explicate the mechanisms that underlie prediction of learning. Chapter 4 will describe

this follow-up study.

Our hypothesis about nonheme iron as the underlying physiological basis of the learning-prediction information of the time-averaged T2* signal (and hence the role of nonheme iron in learning in healthy young adults) will also be presented in detail and discussed in Chapter 4.

In Chapter 5, some future directions for applying this finding as well as suggestions for overcoming some limitations in our studies will be discussed. Chapter 5 will end with a conclusion summarizing all of the main points of our findings as well as their practical implications.

CHAPTER 2

MOTIVATION AND BACKGROUND

2.1 Motivation

As society develops, individuals and organizations that want to be successful are always under pressure to become more knowledgeable and skillful. That leads to an inevitable need/desire: how to learn and so train new skills effectively. As a matter of fact, in the last few decades, a vast literature has been generated on learning mechanisms and effects of training. Indeed, effects of training regime are often assessed through participants' learning outcomes. Nevertheless, there are substantial individual differences in the effectiveness of different training programs for different individuals. Understanding individual differences in learning and training will not only help in designing effective training regimens or intervention but also will likely have important implications for selection of individuals for different training programs.

In our study about training and effects for the Office of Naval Research (ONR), we use a video game training to study training strategies as well as their transfer benefits. While video game skills have been shown to transfer to other tasks [12, 13], influence of individual differences in learning complicates the interpretation of these effects

In short, it is important to be able to evaluate individual differences. And hence, we would like to predict how much individual differences contribute to learning outcomes. Particularly, we want to predict how much future improvement each trainee would gain based on data collected before training begins.

Specifically, we applied multi-voxel pattern analysis on time-averaged T2*-weighted images to predict performance improvements in our video game

training studies. Indeed, the proportion of the variance among individuals obtained by our predictor was much higher than those in other cognitive test prediction [3] or in other imaging studies which looked at BOLD activations [14, 15] or even volume of region of interest [4].

Furthermore, in comparison to behavioral cognitive tests, these images are more direct measurements of neuroanatomy and neurofunction while in fact individual differences in cognitive abilities stem from these brain physiology variations. In other words, it allows more understanding about the neurophysiology of learning mechanism. Truly, the high accuracy in learning prediction of information in time-averaged T2*-weighted images as well as its potential of building a neuromarker for learning led us to a follow-up study designed to explore the mechanisms behind the learning prediction information in time-averaged T2*-weighted images.

2.2 Region of interest: the striatum

In our analysis we focused on the dorsal striatum, consisting of the caudate nucleus and the putamen, and on the nucleus accumbens in the ventral striatum because of these structures' involvement in learning and execution of complex responses. Indeed, the dorsal striatum has been shown to play an important role in procedural and habit learning and in carrying out or initiating complex goal-directed tasks such as task-switching or reaction-time tasks [16, 17, 4, 18, 19, 20, 21]. The ventral striatum, typically related to reinforcement and motivation [19, 22, 23], is also recruited during learning [24, 25, 26]. Both the dorsal and ventral striatum show increased release and binding of dopamine, which has been associated with better performance in learning including video game training [27, 28, 29, 30]. Particularly, an increase in the functional activity in the striatum has been associated with the transfer of updating skills in working memory (an important component of learning performance) tasks, possibly regulated by dopaminergic modulation [31, 32].

Actually there is a co-localized relationship between dopamine and brain nonheme

iron; i.e., they have similar distribution maps in the brain [33, 34]. They both are found with high concentration at regions such as globus pallidus, putamen, caudate, hippocampus, etc. Indeed, brain nonheme iron also plays a crucial role in learning via its effects on dopamine functioning and metabolism dopamine [35, 36, 37, 38]. Other relations of brain iron with learning are via its effects on, for example, hippocampus integrity [39, 40, 41] and myelination regulation [42].

2.3 Pattern recognition - support vector regression

Pattern recognition entails the use of computer algorithms to automatically discover regularities of input data $\mathbf{x}$ in order to generate some sort of outputs $\mathbf{y}$ (labels or discrete values for classification, continuous variables for regression). For a machine to know how to decide on output labels/values, i.e. to build the mapping model $\mathbf{x} \mapsto \mathbf{y}$, it has to be trained. In the case of supervised learning, the training process involves learning the answer from a training data set $\{\mathbf{x}_0, \ldots, \mathbf{x}_N\}$ with known corresponding output values $\{\mathbf{y}_0, \ldots, \mathbf{y}_N\}$. Target values of training data sets are unknown in the case of unsupervised learning, or a mixture of known and unknown target for the case of semi-supervised learning. After the training period (learning phase), the model of mapping $\mathbf{x} \mapsto \mathbf{y}$ is obtained and for any new-coming instance $\mathbf{x}_t$ (testing data); its corresponding output $\mathbf{y}_t$ can be generalized from the learned model. This step is known as generalization.

In our studies, the pattern recognition problem is a supervised one. Particularly from measured MR signals of participants' brains ($\mathbf{x}$), we would like to learn regularities related to participants' video-game learning (continuous variable $\mathbf{y}$). We chose to use support vector regression as it has been applied successfully in many other practical applications [43, 44]. The following section provides background for support vector regression.

Support vector regression (SVR) [45, 46] is a machine learning technique learning the functional relationship between two types of data, $\mathbf{x}$ and $\mathbf{y}$, with a maximum

margin criterion. Specifically, the goal is to use training data $\{(\mathbf{x}_1, \mathbf{y}_1), \ldots, (\mathbf{x}_N, \mathbf{y}_N)\} \subset R^d \times R$ to find the coefficients $\mathbf{w}$ and offset b of a linear function $f(\mathbf{x}) =< \mathbf{w}, \mathbf{x} > +b$ ($\mathbf{w} \in R^d$ and $b \in R$) so that flatness of the coefficients $\mathbf{w}$ is maximized - equivalent to minimizing $||\mathbf{w}||^2$, and so that no error is greater than the limit : $|\mathbf{y}_i - f(\mathbf{x}_i)| \leq \varepsilon$ (for ε-SVR).

However, in order to solve the optimization problem this error condition is relaxed by allowing some error ξ_i ("soft margin"), which is then penalized in the optimization. In short, we would like to solve the following optimization problem:

Minimize $\frac{1}{2}||\mathbf{w}||^2 + C \sum_{i=1}^{l} (\xi_i + \xi_i^*)$

Subject to

$$\begin{cases} \mathbf{y}_i - < \mathbf{w}, \mathbf{x}_i > -b \leq \varepsilon + \xi_i \\ < \mathbf{w}, \mathbf{x}_i > +b - \mathbf{y}_i \leq \varepsilon + \xi_i^* \\ \xi_i, \xi_i^* \geq 0 \end{cases}$$

where $C > 0$ measures the trade-off between the flatness of $\mathbf{w}$ and the tolerance for deviations greater than ε.

The equivalent dual formulation of this primal objective function using Lagrange multipliers is easier to solve:

Maximize

$$-\frac{1}{2} \sum_{i,j=1}^{l} (\alpha_i - \alpha_i^*)(\alpha_j - \alpha_j^*) < \mathbf{x}_i, \mathbf{x}_j > -\varepsilon \sum_{i=1}^{l} (\alpha_i - \alpha_i^*) + \sum_{i=1}^{l} \mathbf{y}_i (\alpha_i - \alpha_i^*)$$

subject to $\sum_{i=1}^{l} (\alpha_i - \alpha_i^*) = 0$ and $\alpha_i, \alpha_i^* \in [0, C]$, where $\alpha_i, \alpha_i^* \geq 0$ are Lagrange multipliers. Solving the dual optimization problem, one obtains:

$$\mathbf{w} = \sum_{i=1}^{l} (\alpha_i - \alpha_i^*) \mathbf{x}_i$$

and

$$b = \begin{cases} \mathbf{y}_i - < \mathbf{w}, \mathbf{x}_i > -\varepsilon, \text{ for } \alpha_i \in (0, C) \\ \mathbf{y}_i - < \mathbf{w}, \mathbf{x}_i > +\varepsilon, \text{ for } \alpha_i^* \in (0, C) \end{cases}$$

Note that α_i and α_i^* cannot be simultaneously non-zero.

As in any machine learning technique, generalization of the model parameters derived from the training data to an independent validation data set is not guaranteed. Although the true error in SVR cannot be always calculated, its upper bound has been shown to be the sum of the training error and the complexity of the sets of models. For the set of hyper planes $f(\mathbf{x}) =< \mathbf{w}, \mathbf{x} > +b$, minimizing model complexity is equivalent to minimizing $||\mathbf{w}||^2$. Hence, SVR allows for the derivation of the function $f(\mathbf{x})$, which achieves the lowest bound of the true error.

Leave-one-out procedure

To avoid biases in the training process, the available data have to be partitioned into non-overlapping training and validation sets. This associated process of splitting the data for training and evaluating learning is known as cross validation. Here we split the data allowing only one observation to be in the validation set. This special case of cross validation is called leave-one-out. Although this method is computationally expensive, it allows for all data to be used for training and validation in turn, while maintaining integrity of the separation of training and validation sets, thus avoiding biases in the modeling. Note that in our application, original MR signals have to be pre-processed before entering prediction stage and it is important to process MR data of all participants (including testing and training ones) with the same procedure.

2.4 Magnetic resonance signal generation and detection

Well-known for its high degree of safety and ability to provide a variety of imaging contrasts including different quantitative measurements, MRI has been very popular in the past few decades, for use in a variety of domains including clinical diagnosis, psychology and neuroscience. Indeed, our studies have used it as the imaging technique for exploring the neurophysiology of learning in young adults. In [47], we used gradient-echo EPI and MPRAGE to measure the BOLD fMRI signals and high-resolution T_1-weighted structural data, respectively, and discovered the high

prediction power of time-averaging T_2^*-weighted signals in predicting the learning of young adults in the Space Fortress video game-training study. In order to discover the mechanism(s) underlying the prediction of time-averaging T_2^*-weighted, a follow-up study collected multiple MR modality signals including diffusion tensor imaging (DTI), arterial spin labeling (ASL), susceptibility weighted imaging (SWI), T_2-quantitative, T_2^*-quantitative, T_2-weighted, and of course T_2^*-weighted (BOLD-EPI) and T_1-weighted measurements. The purpose of this section is to provide the basic principles of MRI signal generation.

2.4.1 The strong external magnetic field $\vec{B_0}$

A nucleus with non-zero spin I (nuclear spin quantum) such as ^1H creates a microscopic magnetic field which is represented by the nuclear magnetic moment vector $\vec{\mu}$ [48]. The spin quantum and the magnitude of the magnetic moment $\vec{\mu}$ are related by the following equation:

$$\mu = \gamma\hbar\sqrt{I(I+1)}$$

On macroscopic scales, however, without an external magnetic field, due to the random direction of $\vec{\mu}$ at thermal equilibrium, there is no net magnetic field. Only in the presence of a strong external static magnetic field$\vec{B_0}$ (without loss of generality, assume $\vec{B_0}$ is in the z-direction), $\vec{\mu}$ has:

- Longitudinal component μ_z: $\vec{\mu}$ has a quantized value along the direction of $\vec{B_0}$

$$\mu_z(t) = \mu_z(0) = \gamma m_I \hbar$$

  where γ is the gyromagnetic ratio constant; m_I is the magnetic quantum number and can take only $(2I+1)$ discrete values, i.e. $m_I = -I, -I+1, \ldots, I$.

With respect to $\vec{B}_0$, $\vec{\mu}$ points up or down at the angle θ:

$$\theta = \pm\frac{\mu_z}{\mu} = \pm\frac{m_I}{\sqrt{I(I+1)}}$$

- Transverse component $\mu_{xy} = \mu_x\vec{x} + \mu_y\vec{y}$: $\vec{\mu}$ has a random phase in the transverse plane and precesses about the $\vec{B}_0$ direction at an angular frequency called the Larmor frequency:

$$\omega_0 = \gamma \mathrm{B}_0 \tag{2.1}$$

Particularly,

$$\mu_{xy}(t) = \mu_{xy}(0)e^{-i\gamma B_0 t}$$

where $|\mu_{xy}| = \sqrt{\mu^2 - \mu_z^2} = \gamma\hbar\sqrt{I(I+1) - m_I^2}$.

As a result of random phases of the microscopic transverse components of each magnetic moment vector, at equilibrium in the presence of $\vec{B}_0$ the net macroscopic magnetization

$$\vec{M} = M_x\vec{x} + M_y\vec{y} + M_z\vec{z} = \sum_{n=1}^{N_s}\mu_{x,n}\vec{x} + \sum_{n=1}^{N_s}\mu_{y,n}\vec{y} + \sum_{n=1}^{N_s}\mu_{z,n}\vec{z}$$

has the same direction as B_0 and $\vec{M} = \sum_{n=1}^{N_s}\mu_{z,n}\vec{z}$ (i.e. transverse component is canceled out).

Particularly:

$$\left|\vec{M}\right| = M_z^0 = \frac{\gamma^2\hbar^2 B_0 N_s I(I+1)}{3KT_s}\vec{z}$$

where K is the Boltzmann constant, T_s is the absolute temperature of the spin system and N_s is the total number of spins in both states.

2.4.2 Radio-frequency oscillating magnetic field $\vec{B_1}$

Despite the non-zero value of the bulk magnetic field, this bulk magnetization cannot be collected as it is not a time-varying signal. To this end, a Larmor frequency oscillating magnetic field $\vec{B_1}(t)$ is applied to make randomly precessing spins phase coherence. Macroscopically, $\vec{B_1}$ perturbs spins so that $\vec{M}$ is tipped away from the equilibrium z-direction, and the transverse component $\vec{M}_{xy} = M_x\vec{x} + M_y\vec{y}$ is non-zero and oscillates around the z-direction at the Larmor frequency. When $\vec{B_1}$ is turned off, $\vec{M}$ still precesses around the $\vec{B_0}$ direction until it gets back to its equilibrium state, i.e. recovers the longitudinal magnetization at equilibrium M_z^0 (longitudinal relaxation), and the transverse magnetization M_{xy} vanishes (transverse relaxation). This process is referred to as *free precession*.

Time-varying values of $\vec{M}(t)$ can be calculated by the Bloch equation:

$$\frac{d\vec{M}}{dt} = \gamma\vec{M} \times \vec{B} - \frac{M_x\vec{x} + M_y\vec{y}}{T_2} - \frac{(M_z - M_z^0)\vec{z}}{T_1}$$

where $\vec{B} = \vec{B_0} + \vec{B_1}$; M_z^0 is the bulk magnetic value of $\vec{M}$ when there is only $\vec{B_0}$; T1 and T2 are time constants characterizing the relaxation process of the spin systems. For tissues, T2 is always smaller than T1, but they are approximately equal in pure water.

It can be shown that at time t during the duration $[0, \tau_p]$ of applying $\vec{B_1}$, in on-resonance conditions (all isochromats resonating at the same Larmor frequency $\omega_0 = \gamma B_0$), the bulk magnetic $\vec{M}$ are tipped away from the z-direction at the small angle:

$$\alpha = \int_0^t \gamma B_1^e(\hat{t})d\hat{t}$$

When $\vec{B_1}$ is turned off, in the Larmor-rotating frame (x', y', z'), transverse and longitudinal relaxation can be described by the following exponential functions:

$$M_{x'y'}(t) = M_{x'y'}(0+)e^{-t/T_2} \quad (2.2)$$

$$M_{z'}(t) = M_z^0(1 - e^{-t/T_1}) + M_{z'}(0+)e^{-t/T_1} \quad (2.3)$$

where $M_{x',y'}(0+)$ and $M_{z'}(0+)$ are the transverse and longitudinal magnetizations right before $B_1(t)$ is turned off.

These radio-frequency precessing time-varying magnetizations (mainly the transverse ones, i.e. the longitudinal one is ignored due to its much slower time-varying characteristic) induce an electromagnetic force (or voltage) in receiver coils and hence can be detected. Let $\rho(\omega)$ be the spin spectral density function at the precessional frequency ω (in the Larmor rotating frame), the detected free (precession) induction decay signal FID can be written as:

$$S(t) = \int_{-\infty}^{\infty} p(\omega) e^{-t/T_2} e^{-i\omega t} d\omega \tag{2.4}$$

For example, for the application of an α pulse (i.e. $\vec{B_1}$ tips $\vec{M}$ an angle α away from the $\vec{B_0}$ direction), signal $S(t)$ detected from a spin system resonating only at the single frequency ω_0 (i.e. $\rho(\omega) = M_z^0 \delta(\omega - \omega_0)$) bears characteristic T_2-decay as follows:

$$S(t) = M_z^0 sin(\alpha) e^{-t/T_2} e^{-i\omega_0 t}$$

However, in the case of field inhomogeneity (the sample and/or the magnetic field are not homogeneous), the signal decay is characterized by a new time constant T_2^* with $\frac{1}{T_2^*} = \frac{1}{T_2} + \gamma \Delta B_0$. For Lorentzian distribution of the spectral density function $\rho(\omega) = M_z^0 \frac{(\gamma \Delta B_0)^2}{(\gamma \Delta B_0)^2 + (\omega - \omega_0)^2}$, the FID signal S(t) is as follows:

$$S(t) = \pi M_z^0 \gamma \Delta B_0 sin\alpha e^{-t/T_2^*} e^{-i\omega_0 t}$$

2.4.3 Gradient magnetic field $\vec{B_G}$

When imaged objects are in the strong and uniform $\vec{B_0}$ and excited by radio-frequency (RF) oscillating magnetic field $\vec{B_1}$ only, spins from all parts of the objects are activated; i.e., the detected signal is the sum of all of the signals from all parts of the subjects. To activate the signals from the different parts of the imaged objects requires spatial localization comprising of two separate steps: selectively exciting an imaged

region and the spatial information encoding as follows:

- Slice selection: Recall that the RF pulse $\vec{B_1}$ can only be frequency-selective. For a given excitation RF pulse, if the resonance frequencies of spins are made to be position-dependent, spins at different locations will be excited differently. To this end, the resonance frequency of spins can be spatially varied by corresponding spatial variations of the magnitude of $\vec{B_0}$. Particularly, for the purpose of slice selection, a magnetic field (of the same direction as $\vec{B_0} = B_0\vec{z}$) called a slice selection gradient field, having an amplitude that changes linearly along the slice selection direction $\vec{B_G}(x, y, z) = (G_x x + G_y y + G_z z)\vec{z}$ is added into the homogeneous magnetic field $\vec{B_0}$. Spatial variation of the magnetic field therefore will be $\nabla B = G_x\vec{x} + G_y\vec{y} + G_z\vec{z} \equiv \vec{G_{ss}}$ ($\vec{G_{ss}}$: slice selection gradient). With the presence of the gradient $\vec{G_{ss}}$, the desired slice profile can be obtained by carefully designing the excitation frequency and the shape of the RF pulse $\vec{B_1}$.

- Spatial information encoding: after the excitation of the (slice-selective or non-selective) RF pulse (i.e. in the remaining homogeneous B_0 field and a gradient magnetic field, for example, $B_G = G_x x + G_y y + G_z z = \vec{G_{fe}} \cdot \vec{r}$), the Larmor frequency at position $\vec{r} = (x, y, z)$ is $\omega(x, y, z) = \gamma B_0 + \gamma\vec{G_{fe}} \cdot \vec{r}$ and the activated signal collected during the free-precession period is in a complex exponential form similar to equation 2.4:

$$S(t) = \int_{-\infty}^{\infty} \rho(\vec{r}) e^{-i(\gamma B_0 + \gamma\vec{G_{fe}} \cdot \vec{r})t} d\vec{r}$$

  (omitting the transverse relaxation effect e^{-t/T_2}).
  It is clear from the above equation that if a gradient $\vec{G_{fe}}$ is turned on after the RF pulse excitation, signal at location x will dephase at a position-dependent frequency $\omega(x) = \gamma B_0 + \gamma\vec{G_{fe}} \cdot \vec{r}$. This procedure is known as *frequency encoding*.
  Besides frequency encoding, there is also *phase encoding*: right after the RF

pulse, if G_{pe} is turned on for a short time $[0, T_{pe}]$, the local signal at different locations will have a different initial phase $\phi(\vec{r}) = -\gamma\vec{G_{pe}} \cdot \vec{r}T_{pe}$. Omit the high Larmor frequency (as it is deplexed by collected coils) γB_0, define $\vec{k} = \frac{\gamma}{2\pi}\vec{G}t$ and map our signal from the time domain to the so-called *k-space* domain, we have:

$$S(\vec{k}) = \int_{\text{object}} \rho(\vec{r})e^{-i2\pi\vec{k}\cdot\vec{r}}d\vec{r} \tag{2.5}$$

2.4.4 RF pulse echo and gradient echo signals

From the above equation 2.5, it is clear that the collected signal in k-space is the sampled data of the Fourier transform of the imaging object of interest. However, for better reconstruction, a symmetric coverage of the sampled signals in k-space is desired. Therefore, two-sided signals, called *echos*, are collected instead of one-sided FIDs.

There are two different ways to obtain echo signals: using multiple RF pulses or magnetic field-gradient reversal.

- RF pulse echo: At time $t = 0$, the excitation α_1-degree RF pulse is turned off, magnetization vectors with different isochromats precess about the B_0 direction at different frequencies. As different isochromats have different precession frequencies, dephasing occurs. Particularly, after a time τ, an isochromat precessing at ω_{slow} will lag behind one precessing at ω_{fast} ($\omega_{\text{fast}} > \omega_{\text{slow}}$) by an angle $(\omega_{\text{fast}} - \omega_{\text{slow}})\tau$. As a result, the magnetization decays at the speed e^{-t/T_2^*} ($T_2^* < T_2$). However, if we apply another α_2-degree RF pulse to flip them over on the transverse plane, given that the rotation direction is unchanged, the ω_{fast} isochromat will become "behind" the other, and their phase lag will progressively decrease (the collected signal regrows). Another time τ after that, the ω_{fast} isochromat will be completely in phase with the ω_{slow} one and as a result of their new phase coherence at $t = 2\tau$ (called echo time T_E), the

collected signal will reach its peak (they are still susceptible to the transverse decay effect e^{-t/T_2} though). After the complete phase coherence at $t = 2\tau$, the dephase progressively increases until the signal vanishes. The collected signal is two-sided and symmetric at echo time with the amplitude peak:

$$A_E = M_z^0 sin\alpha_1 sin^2 \frac{\alpha_2}{2} e^{-\frac{T_E}{T_2}} \tag{2.6}$$

- Gradient echo: After the excitation of the α_1-degree RF pulse $t = 0$, if a negative gradient is applied along the x-direction, for example, dephasing along that direction worsens, and as a result, the signal decays at a faster rate $e^{-t/T_2^{**}}$ ($T_2^{**} < T_2^*$) and reaches zero at time $t > 3T_2^{**}$. At time $t = \tau$, if another positive gradient with the same amplitude/direction is applied, dephasing induced by the negative gradient will gradually disappear and be zero at $t = 2\tau$.
  Correspondingly, the signal strength increases and reaches its peak at $t = 2\tau$.
  The gradient echo signal strength is characterized by e^{-t/T_2^*} (hence, it is weaker than an RF echo signal), and is usually used in fast imaging with small tip-angle excitation.

$$A_E = \frac{M_z^0(1 - e^{-T_R/T_1})}{1 - cos\alpha e^{-T_R/T_1}} sin\alpha e^{-\frac{T_E}{T_2^*}} \tag{2.7}$$

2.4.5 Imaging contrasts

From equations 2.6 and 2.7, it is clear that intensity of the collected signal is indeed a function of spin density, relaxation times T_1, T_2, T_2^*, etc. Furthermore, a given pulse sequence but with a different calibration of parameters (i.e. different choices for the repetition time T_R (duration between the first RF excitation of two consecutive cycles), echo-time T_E, flip-angle values α, etc.) can give a different *contrast* or *weighted-image*.

To understand more about imaging contrast, consider the simple case of a basic saturation-recovery spin-echo pulse sequence, and for $T_R >> T_E$ (as in practice), the

signal intensity can be proved to be:

$$A_E = M_z^0 \left(1 - e^{-T_R/T_1}\right) e^{-T_E/T_2}$$

If the sequence is run with a short T_E value and an appropriate T_R, the term e^{-T_E/T_2} can be approximated by 1 and the signal intensity at different sample locations will mainly depend on their corresponding T_1-values. As longitudinal relaxation time T_1 varies a lot for different soft tissue types, variation in the relative T_1-values results in *contrast* and therefore discrimination between structures (T_1-contrast indeed is very suitable for anatomical brain information acquisition). A collected signal in such a case is said to have T_1-contrast or be T_1-weighted.

If we choose an appropriate T_E but a very long T_R, the term e^{-T_R/T_1} will vanish, leaving the output dependent mostly on e^{-T_E/T_2} and we have a T_2-weighted one.

For a short T_E and long T_R pulse sequence, we will have a proton density weighted image. In practice, as different soft tissues have much the same water-proton concentration, water-proton density-weighted images usually give good contrast between, for example, skull/bone and brain, and are used less often.

Although it is quite similar to spin-echo imaging, gradient-echo imaging which utilizes gradient refocusing can provide more types of imaging contrast, including $T_1-, T_1/T_2-, T_2-$ and especially T_2^*-contrast. In particular, T_1-weighting in gradient echo imaging is controlled by the calibration of both of T_R and the flip angle α. For getting T_2^* from gradient echo imaging, T_E needs to be adjusted.

CHAPTER 3

LEARNING PREDICTIVE INFORMATION IN TIME AVERAGED T_2^* SIGNAL AT BASAL GANGLIA

This chapter describes our previous finding (Vo et al., 2011) that time-averaged T2* MR signals can be used to effectively predict learning, based on information in the dorsal striatum, in the Space Fortress video game. These data motivated the conduct of another study (discussed in Chapter 4) to explicate the mechanisms underlying this successful prediction.

3.1 Experiment design of video game learning study in 2008

3.1.1 Participants

Forty-two participants were recruited from the local communities of Urbana and Champaign, Illinois. All participants were young, right-handed adults between the ages of 18 and 28 with little experience with video games (less than 3 hours per week). Of the 42 participants, 39 completed the experiment, and of those 5 were excluded from the analysis because of incomplete data. The final sample consisted of 34 young adult participants (mean age = 22, SD = 3, 8 males) with normal or corrected-to-normal visual acuity, normal color vision, and normal hearing. At the time of data collection none of the participants were on any medications that might affect cognitive abilities. To be accepted into the study, participants were required to pass an aiming task to ensure that they were able to use the joystick and had little experience in playing video games.

Note that all studies described in this dissertation were approved by the University

of Illinois Institutional Review Board (IRB), and all participants provided written informed consent according to the principles of the Declaration of Helsinki.

3.1.2 Study tool: Space Fortress video game

Those participants were trained to play Space Fortress (figure 3.1), a complex video game developed as a tool to study training strategies, skill acquisition and learning [49, 50].

Figure 3.1: Schematic interface of the Space Fortress video game. The objective of the game is to destroy the space fortress (yellow, center of the display) by shooting missiles at it from a spaceship (yellow, upper-left corner), while moving the spaceship inside the hexagon with thruster commands to evade mines (red diamond) and to collect resources ($-sign).

Playing Space Fortress requires complex procedural learning of second-order motion control in a frictionless environment while simultaneously completing a number of other challenging tasks, including target detection and discrimination, memory updating, and resource management. Total game score is composed of four sub-scores, respectively measuring: 1. control: maneuvering the spaceship in a predefined allowable area (big hexagon in figure 3.1) with thrusters, which amounts to second-order motion control in a frictionless environment without braking system; 2. velocity: keeping the velocity of the spaceship within a predefined range; 3. speed: quickly and accurately handling mines, which can either be friendly or hostile; and 4. points: successfully destroying the fortress with ten missile hits with at least 250ms

separation, while preventing one's own ship from being destroyed by missiles from the space fortress or by a mine. In parallel with controlling the spaceship, maintaining velocity, and handling mines and missiles, players always needed to monitor a stream of symbols for a dollar sign ($), whose second appearance indicates a bonus in the form of extra missiles or game points. In addition, players needed to retain three letters in their working memory that identified mines as friendly or hostile. The sum of these four sub-scores served as a measure of a subject's performance.

3.1.3 Training procedure

Once participants passed the aiming test, and they watched an instructional video on how to play Space Fortress. After a minimal amount of practice to ensure they understood the operation and objectives of the game, participants played four 4-minute blocks of Space Fortress as part of a two-hour MRI session in a 3-Tesla Siemens Allegra MRI scanner (the first MRI session). The total game score during this first session inside the scanner was used as a measure of participants' abilities prior to extensive training.

Subsequently, over the course of the next three to eight weeks (38 days on average) participants completed ten two-hour training sessions playing Space Fortress outside the scanner (figure 3.2). Each of training session consisted of 36 three-minute games.

After participants finished the training period, they underwent another MRI session identical to the first (the second MRI session). Total game score during this second session inside the scanner reflects participants' abilities after extensive training. Note that imaging data from the second MRI session are not used; i.e., only MR data from the first session are used to predict learning outcome.

3.1.4 Learning measurement

The score improvement from the first to the second MRI session, i.e., the difference between the game scores in MRI sessions 2 and 1, served as a measure of individual

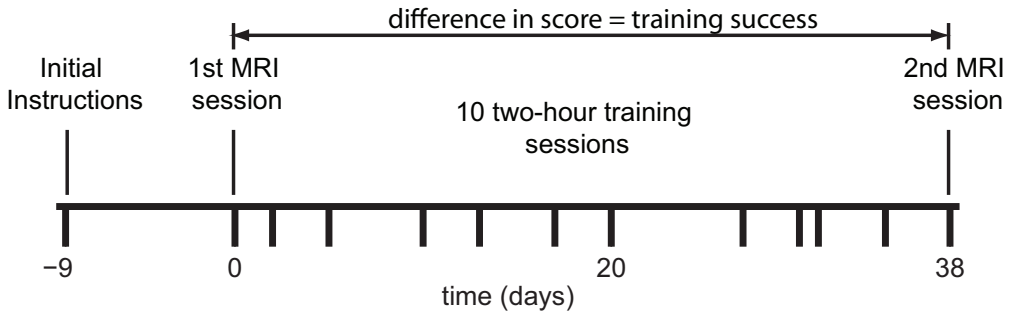

Figure 3.2: Timeline of the experiment for a typical participant. After initial instructions, participants played Space Fortress in the MRI scanner while their brain activity was recorded. Next, participants underwent a total of 20 hours of training, followed by a second MRI session. We used the difference in total game score between the two MRI sessions (i.e. the score improvement) as a measure of learning success.

learning success. Note that we only consider game performance during the two MRI scans, since the main focus is on predicting learning success from imaging data. For details of the progression of training outside the scanner see reference [51].

Also, it is not straightforward to compute relative (e.g., percent) improvement, since game scores can be negative, and adding a constant offset to the score is bound to be arbitrary. We have attempted to compute relative score improvements by computing percentile ranks (R) for the game scores at time 1, and then using the mean and variance of time 1 scores to compute the percentile ranks at time 2. Relative score improvement was computed as $\frac{R_{\mathrm{time\,2}} - R_{\mathrm{time\,1}}}{R_{\mathrm{time\,1}}}$. However, due to the transformation to percentiles, the relationship between this relative score improvement and the absolute score improvement is non-linear. Relative score improvements computed in this manner are not predicted as well by T_2^* activity in the dorsal striatum as absolute score improvements.

3.1.5 Imaging session design

MR images were acquired by a 3T Siemens Allegra. At each session, for each subject, the following data were collected:

- T_1-weighted high-resolution structural volume (voxel size $1.33 \times 1.33 \times 1.30$mm, $160 \times 192 \times 144$ voxels). Using MPRAGE sequence.

- Thirteen blocks of T_2*-weighted EPI images: echo time $TE = 25$ms; repetition time; flip angle $\alpha = 80^0$. Each volume included 28 slices at 64×64 voxels each (voxel size: $3.4375 \times 3.4375 \times 4$mm).

  The 13 blocks consisted of seven 46-second blocks of passively watching (PW) a sample video game played by an expert, interleaved with six active blocks. The six active blocks included two blocks of an odd-ball task (OB), which required counting the number of high-pitch tones among low-pitch distracting ones, two blocks of playing the Space Fortress game (SF block), and two blocks of playing Space Fortress while also performing the odd-ball tasks (SO block). Each active block was four minutes long. The 13 blocks were arranged in the following order: PW-OB-PW-SF-PW-SO-PW-SO-PW-SF-PW-OB-PW.

3.2 Learning predictive information from pattern of time-averaged T_2^* at basal ganglia

3.2.1 Pre-processing of imaging data

Slice-timing correction

Each volume in the T_2^*-w EPI series takes a TR=2s to collect, so for data within the same volumes to appear as having been collected simultaneously, slice-timing corrections at each voxel location are needed. A simple way to implement this is by shifting the phases of the data in the frequency domains (which is not k-space data but the Fourier transformation of the time series).

Motion correction

In MR data acquisition, especially when collecting a series of BOLD images, subjects usually make involuntary head movements despite the use of motion-restricting pads. In our analysis, although a small percentage of the signal-intensity changes at each voxel location over the time course of the stimuli are not examined as in a typical BOLD imaging study, a voxel-wise alignment of the EPI data collected during each block is still necessary. Particularly, motion-induced rigid displacement is undone by affine transformation (assume no other head-motion-induced effects such as in [52]). Indeed, for fast and robust motion correction, we use the mcflirt tool [53]. See figure 3.3.

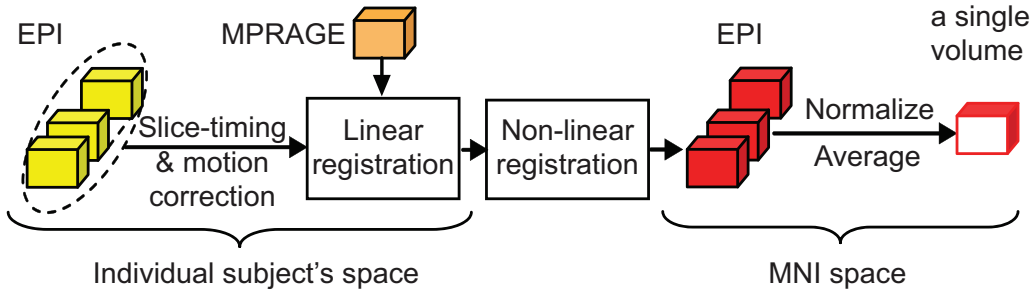

Figure 3.3: MRI preprocessing workflow. EPI volume series (1st MR session) of different subjects are registered to the common space (MNI space) by linear and non-linear registration. After normalization, temporal averages of the EPI volumes are used for the subsequent analysis.

Linear and non-linear image registration

To extract data of many subjects at the same ROIs, it is necessary to transfer all data of each individual into a common space such as MNI (Montreal Neurological Institute) space. Specifically, high-resolution structural T_1 volume acquired for each participant during MRI session 1 was nonlinearly registered into MNI space using FNIRT tool of FSL package with output of affine registration (using FLIRT) as initial guess [54, 55]. T_2*-weighted volumes of the 1st MR session were also non-linearly registered to MNI

space through a concatenation of their linear transformation to same-subject T_1 volume and the non-linear wrapping of that structural volume into MNI space. After being transformed into MNI space, data were re-sampled back to the resolution of the original EPI scans ($3.4375 \times 3.4375 \times 4$mm). Also note that for our analysis target, no explicit spatial smoothing was applied and anatomical structures in the striatum were identified based on brain atlases included with the FSL analysis software [56].

This registration was followed by a normalization step to account for variations of scanner settings between runs. Particularly, activity in each EPI volume was divided by the mean activity in the brain of this volume to compensate for drift in scanner adjustments and differences between MRI runs and between subjects. This normalized activity was averaged over the four blocks (16 minutes) of active game play (two SF blocks and two SO blocks, 480 volumes in total) and thus some noise as well as signal variations due to functional activity might be suppressed. Note that, as a control, the analysis was repeated with data from the two OB blocks as well as from the seven PW blocks.

Generally speaking, besides the structural T_1-weighted data, for each subject we had one brain volume with the T_2^*-weighted signal aggregated over the entire period of game play inside the MRI scanner as well as the score improvement for these games. And we then performed two different types of region-of-interest (ROI) based analysis with this average T_2^* signal to predict subjects' score improvement: spatial mean activity analysis and multi-voxel pattern analysis (MVPA). Unlike the spatial mean analysis, MVPA utilizes the distributed pattern of voxel activity within an ROI.

3.2.2 Predictive information of time-averaged T_2^* patterns at the basal ganglia

Univariate analysis of time-averaged T_2^*

For the spatial mean activity analysis, we averaged the intensity of all voxels inside an anatomically defined region. As a first test, we divided subjects into groups of good

and poor learners based on a median split of their score improvements. We found significantly higher mean activity for good than poor learners in the dorsal striatum ($p = 0.011$), but not in the ventral striatum ($p = 0.75$, two-sample t tests with $n1 = n2 = 17$). To determine the relationship between subjects' numerical score improvements and mean activity within an ROI we computed their Pearson correlation. In the dorsal striatum, the correlation was significant ($r = 0.47, p = 0.0053$; see figure 3.4), but again not in the ventral striatum ($r = -0.09$).

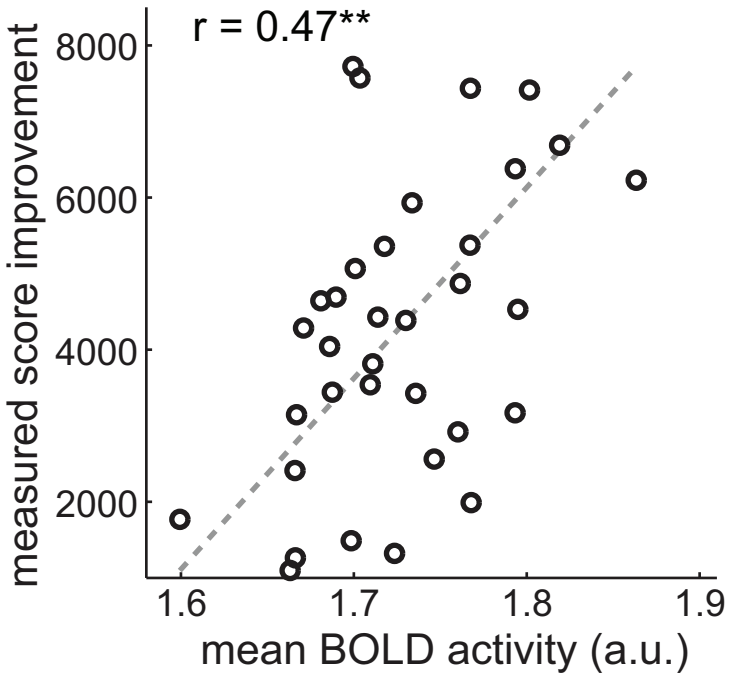

Figure 3.4: Predicting score improvement from MRI activity in the dorsal striatum. Correlation of measured score improvement with the spatial mean of the time-averaged T_2^*-weighted signal in the dorsal striatum. Mean activity of 34 subjects is significantly correlated with score improvement. The dashed lines show the least-squares best linear fits. $**p < 0.01, ***p < 0.001$.

Pattern analysis of time-averaged T_2^* with support vector regression

Although analysis of spatial mean activity can predict score improvements to some extent, it provides merely summary statistics of the activity in an ROI, ignoring subtle differences in activity patterns. Indeed, after subtracting out each individual's average

activity, good and poor learners differed in the multi-voxel patterns of time-averaged T_2^* activity in the dorsal striatum (figure 3.5). The color patches in figure 3.5 suggest a subdivision of the dorsal striatum roughly along the anterior-posterior line. In other words, good and poor learners not only differ in their level of mean activity in the dorsal striatum, but also in the local activity patterns within the dorsal striatum. These differences allow us to predict learning success for individual participants from the patterns of the temporally compounded EPI images recorded at the beginning of training with much higher accuracy than from the spatial mean of activity alone. To

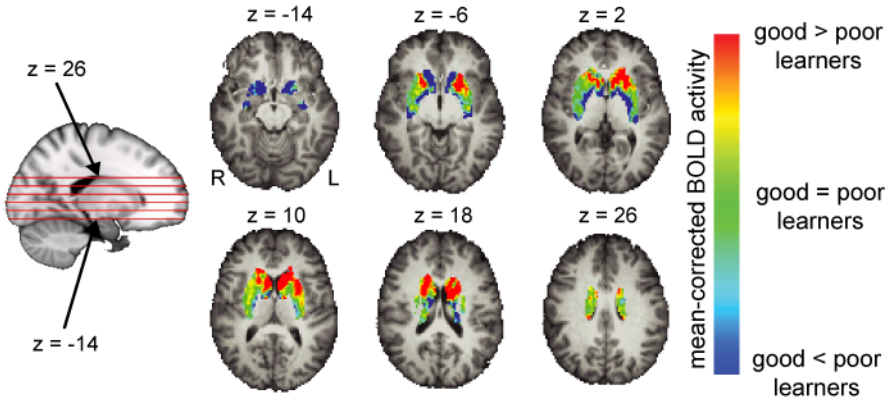

Figure 3.5: Pattern of differences between good and poor learners. Differences in activation patterns in the dorsal striatum between good and poor learners overlaid on top of six anatomical slices with z-coordinates respectively, -14, -6, 2, 10, 18, and 26. For this visualization the group of 34 subjects was split into 17 good and 17 poor learners based on the median of score improvements in Space Fortress over the course of 20 hours of training. Each subject's mean activity was subtracted from her or his activity in the dorsal striatum. The activity patterns were then averaged separately for good and poor learners. The figure shows the difference between the average patterns of good and poor learners.

exploit these differences in a multivariate analysis, we first excluded data from one subject and used activity patterns of the voxels from the remaining subjects, together with their score improvements, to train a support vector regression (SVR) algorithm [45, 46]. The algorithm then generated a prediction for the performance improvement of the excluded subject from her or his pattern of time-averaged T_2^*-weighted activity. The procedure was repeated so that each subject was excluded once in a leave-one-subject-out (LOSO) cross validation procedure, thereby generating

predictions for each subject based on the performance and activity patterns of the other subjects. Details about the SVR algorithm and the LOSO procedure can be found in section 2.3.

The algorithmically predicted score improvements were then correlated with the actual performance improvements in Space Fortress to determine the prediction accuracy. Figure 3.6 shows that the predictions based on pre-training activity patterns in the dorsal striatum were highly correlated with the actual improvements that resulted from 20 hours of training (Pearson correlation coefficient $r = 0.74$, $p = 6.1 \cdot 10^{-7}$). Activity patterns before training accounted for more than half of the variance ($R^2 = 0.55$) among individuals in how much they benefited from training. This represents a substantial improvement in prediction accuracy compared with the spatial mean analysis over the same regions of interest, which explained less than a quarter of the variance (22%; $r = 0.47$; figure 3.6).

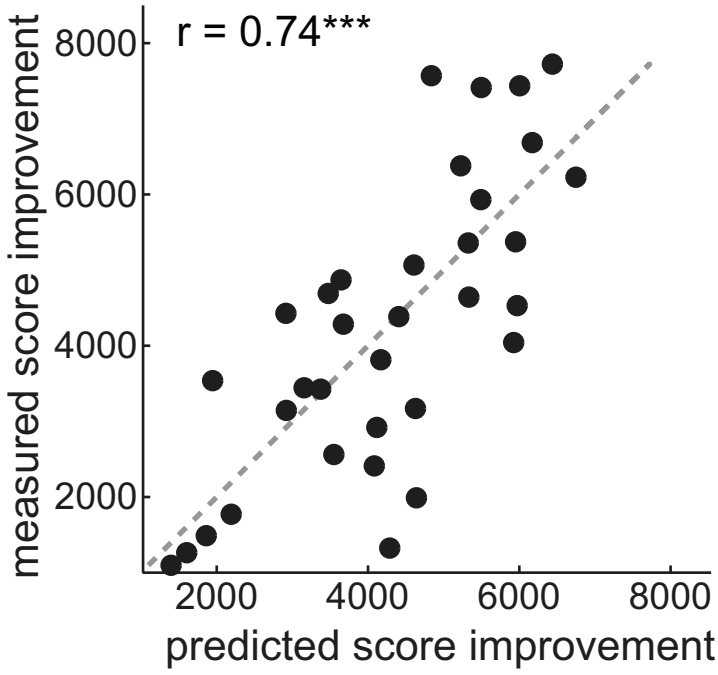

Figure 3.6: Predicting score improvement from MRI activity in the dorsal striatum. Correlation of measured score improvements with score improvement predicted from multi-voxel patterns of the T_2^*-weighted signal in the dorsal striatum. It shows an even higher correlation than in figure 3.4. The dashed lines show the least-squares best linear fits. $**p < 0.01, ***p < 0.001$.

Within the dorsal striatum, predictions based on the pattern of activity in the caudate nucleus ($r = 0.77, p = 1.3 \cdot 10^{-7}$) were more accurate than those based on activity in the putamen ($r = 0.47, p = 0.0046$; figure 3.7), with a marginally significant difference ($p = 0.051$). Furthermore, the left dorsal striatum ($r = 0.80$, $p = 1.0 \cdot 10^{-8}$) showed significantly higher ($p = 0.0037$) predictive power than the right dorsal striatum ($r = 0.36$ significantly, $p = 0.039$). Since all subjects were right-handed and controlled the movements of the spaceship with their right hand, this may be related to motor learning in the contralateral (left) hemisphere. In contrast to good predictions from the dorsal striatum, predictions based on activity patterns in the ventral striatum (nucleus accumbens) were not significantly correlated with measured score improvements ($r = 0.08$).

The score of the Space Fortress game was composed of four sub-scores: *Control* of the spaceship's position; maintaining ship *Velocity* within a predefined range; *Speed* with which subjects discriminated between and responded to different types of mines; and *Points* for successfully destroying the fortress. We repeated the SVR analysis separately for each of the sub-scores. As shown in figure 3.8, the speed sub-score shows the same pattern of results as the total score, including the high correlation of predicted and measured score improvement in the left but not the right dorsal striatum, the higher correlation in the caudate nucleus than the putamen, and the low correlation in the ventral striatum (nucleus accumbens). This suggests that learning success with respect to discrimination and working memory (needed to identify a mine as friendly or hostile and to react to it quickly) is best predicted by time-averaged T_2^* activity in the dorsal striatum. Improvement in motor control, which is reflected in the control and velocity sub-scores, is not predicted to the same extent by the dorsal striatum, although both of these sub-scores are predicted at some level by T_2^* activity in the left nucleus accumbens. Improvements in the points sub-score are not predicted by activity in the striatum, except for a small but significant correlation of predicted and measured score improvement in the left caudate nucleus.

Previously, striatal brain volume was reported to predict score improvement to some extent [4], and volume of an area and its time-averaged T_2^* signal may be related.

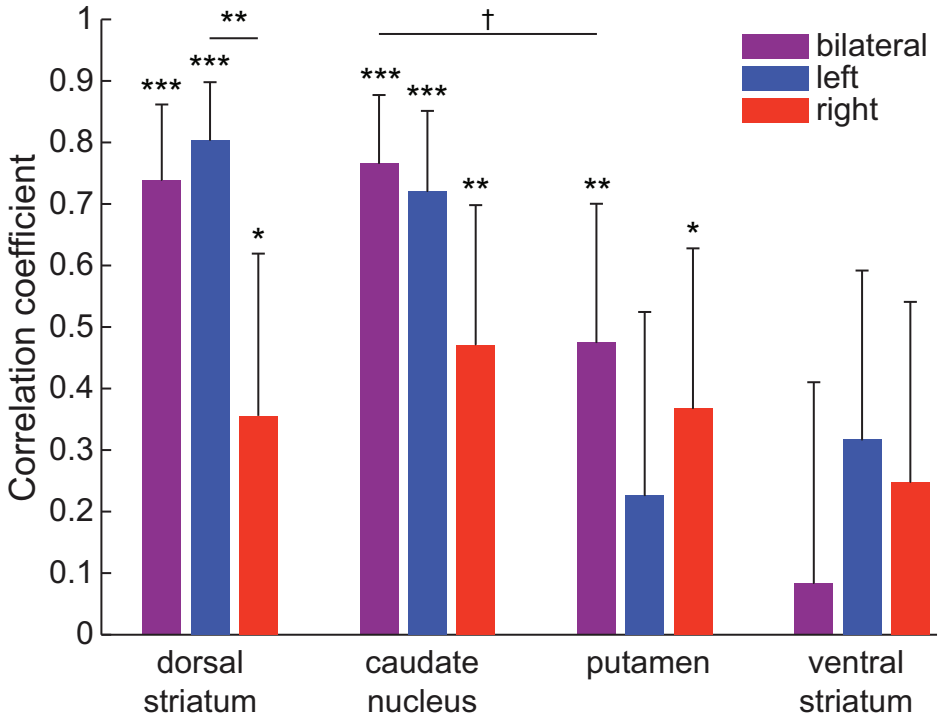

Figure 3.7: Accuracy of predicting individual score improvement from MVPA of the time-averaged T_2^*-weighted signal. In the dorsal striatum, correlation of predicted and measured score improvement for 34 subjects was highly significant. Within the dorsal striatum, correlation for pattern analysis was just as high in the caudate nucleus, but lower in the putamen. Predictions were even less accurate in the ventral striatum (nucleus accumbens). In the dorsal striatum, predictions were significantly more accurate based on activity patterns in the left than in the right hemisphere. The caudate nucleus showed similar lateralization, whereas the putamen did not show strong lateralization. $\dagger p = 0.051, *p < 0.05, **p < 0.01, ***p < 0.001$.

Another potential predictor for score improvement could be the initial score from the games played during the first MRI session. On the one hand, participants with high initial scores may already have reached ceiling performance, showing little further improvement. On the other hand, higher initial score could indicate higher cognitive abilities, enabling participants to benefit more from extensive training. To account for these factors, we used the volume of regions as reported in [4] and the initial score as two additional explanatory variables (covariates) of measured score improvements, in addition to the score improvements predicted by the SVR analysis. We used a second-order partial correlation analysis for each of the three explanatory variables to assess the unique predictive power of each of them irrespective of the other two. Table

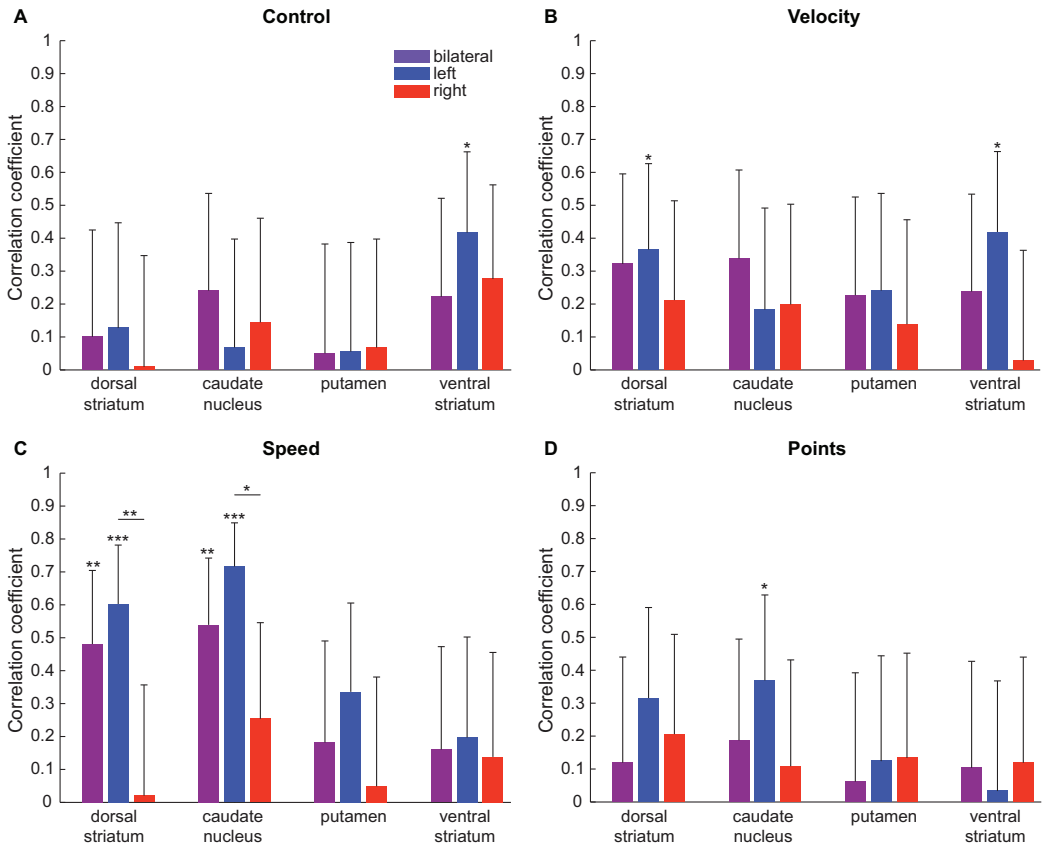

Figure 3.8: Accuracy of predicting improvements in sub-scores from the time-averaged T_2^*-weighted signal. (A) Improvement in the control sub-score is predicted to a limited extent by the time-averaged T_2^* activity in the left ventral striatum (nucleus accumbens). (B) The velocity sub-score shows small but significant correlations in the left caudate nucleus and the left nucleus accumbens. (C) Improvement in the speed sub-score is predicted highly significantly by time-averaged T_2^*-weighted activity in the dorsal striatum, in particular the caudate nucleus, but not by the ventral striatum. Correlation of predicted and measured score improvements is higher in the left than the right hemisphere. This pattern of results matches that of the total score shown in figure 3.7. (D) The points sub-score shows no significant prediction except for a small but significant correlation of predicted and measures score improvement in the left caudate nucleus.
$*p < 0.05, **p < 0.01, ***p < 0.001$.

3.1 shows the correlation of the SVR prediction with measured score improvement to be highly significant, even after removing the effects of striatal volume and initial score. Note that for this analysis, only those 32 of our 34 subjects were used for whom the volumetric data were available from [4]. Also, one might wonder about the use of improvement in game score during the first MRI session (e.g., from game 1 to game 4)

as another predictor. However, we found no significant correlation between improvement within the first MRI session and the improvement from the first to the second MRI session ($r = -0.17$).

Table 3.1: Zero and second order partial correlations. Zero (Pearson correlation) and second-order partial correlations are calculated for a linear regression model with measured score improvements as the predicted variable and three explanatory variables: score improvement predicted by the SVR algorithm from time-averaged T_2^*-weighted activity in the dorsal striatum, volume of the dorsal striatum, and initial score.

Explanatory Variables	Zero-order Pearson correlation (no covariates)	Second-order partial correlation (two covariates)
SVR	0.73 ($p = 1.810^{-6}$)	0.72 ($p = 3.710^{-6}$)
Volumetric data	-0.12 ($p = 0.5$)	0.06 ($p = 0.7$)
Initial score	-0.23 ($p = 0.2$)	-0.09 ($p = 0.6$)

Recall that the brain receives, processes and outputs information through electrochemical conduction with information transferred/received between neurons by neurotransmitters and receptors. These neural activities come at the cost of energy utilization. This means that in the activated brain regions, more oxygen and glucose are consumed. Although there is no simple relationship between brain energy metabolism and blood flow to the regions, there is nevertheless an increase in the blood flow to the activated regions as well as in the relative proportion of oxygen in the blood (in the form of oxygenated hemoglobin, since free oxygen is not actually soluble in the blood). Hemoglobin contains iron which by itself is a paramagnetic element; however, it indeed becomes diamagnetic whenever oxygen binds to it. Since de-oxygenated hemoglobin increases the local magnetic flux or magnetic susceptibility of blood vessels relative to the surrounding brain tissue, the resultant local field gradients lead to the loss of phase coherence of the spins of tissue-water around the blood vessels, and hence decrease T_2^* locally. Therefore, if we use a T_2^*-weighted gradient-echo sequence, the relative blood oxygenation accompanying neuronal activation in the brain [57], i.e. blood oxygen-dependent (BOLD) contrasts,

can be captured. In our experiment, we originally recorded these BOLD-contrasts and the T_2^*-weighted EPI images that are used for functional MRIs. But it is important to emphasize that the time-averaged EPI volumes that we used for our MVPA analysis are unlikely to be functional, because here we are considering the part of the EPI images that is common across the time course rather than modeling the differences in BOLD activity from different stimulus conditions. Therefore, our signal is more likely to capture individual differences in some aspects of neuroanatomy or persistent physiology, such as differences in blood supply to the dorsal striatum or the iron concentration in this region. This view is further supported by the observation that it is not necessary to use the EPI T2*-weighted images recorded during active game play. We obtained almost identical accuracies in predicting score improvement in Space Fortress when we used EPI T2*-weighted images from blocks with an acoustic oddball task ($r = 0.75, p = 2.9 \cdot 10^{-7}$) or from blocks of passively watching Space Fortress games ($r = 0.74, p = 5.6 \cdot 10^{-7}$).

In general, contrasts in MR images are rooted in (and obtained from) many different intrinsic properties of the imaged tissues, such as transverse relaxation time T_2 (or T_2^* in the case of field inhomogeneity) or the longitudinal relaxation time, T_1 (refer to section 2.4 for signal generation and contrast calibration in MRI). To test if we can predict score improvement just as well based on T_1-weighted as T_2^*-weighted images, in MNI space, we normalized and subsampled the MPRAGE images that were acquired during the first scanning sessions to the same resolution as the EPI images (3.4375mm $\times 3.4375$mm $\times 4$mm) and performed the MVPA analysis as described above. Correlation of predicted score improvements with measured score improvement was significantly lower for T_1-weighted than T_2^*-weighted images ($p = 0.031$), although at 0.38 it was still significantly above zero ($p = 0.027$; figure 3.9). The higher prediction accuracy in T_2^* compared to T_1 images might hint at the importance of magnetic susceptibility of the tissue, which affects T_2^* but not T_1. One possible source of susceptibility variations could be iron in the tissues, for instance in supplied blood or brain storage iron [58].

Both white and gray matter contains blood vessels. In the white matter, capillaries

are embedded in the myelin sheaths of axons that project over relatively long distances. In the gray matter, vessels supply mostly the somas and dendrites of neurons. Determining which tissue contributes more to the patterns that let us predict individual learning success could elucidate the anatomical and/or physiological phenomena underlying our effects. We used FSL's FAST automatic segmentation tool [59] to separate white from gray matter in the T_1 image of each individual. We then performed the LOSO cross validation analysis separately on the white matter and on the gray matter voxels figure 3.9. Correlation of predicted with observed score improvement was significantly higher ($p = 0.0026$) in the white matter ($r = 0.65, p = 2.8 \cdot 10^{-5}$) than in the gray matter ($r = 0.02$). This suggests that the long-range, myelinated connections in the white matter are critical for our ability to predict score improvement in Space Fortress.

In figure 3.5 we had noted an apparent anterior/posterior organization of the dorsal striatum based on the difference in activity patterns between good and poor learners. To investigate this organization further, we split the left dorsal striatum in each participant with a coronal plane such that approximately equal numbers of voxels were anterior as posterior of the division. We then repeated the LOSO cross validation analysis separately for the anterior and the posterior half. Prediction accuracy was significantly higher ($p = 0.0024$) from the anterior ($r = 0.82, p = 2.4 \cdot 10^{-9}$) than the posterior ($r = 0.38, p = 0.028$) half of the left dorsal striatum (figure 3.9), accounting for 68% of the variance among individuals. This result substantiates the qualitative observation in figure 3.5 with a quantitative difference between anterior and posterior parts of the dorsal striatum.

3.2.3 Practical implications

In this study we have found that patterns of time-averaged T_2^*-weighted signal in the dorsal striatum recorded before the start of extensive training are highly predictive of individuals' future learning success in a complex video game (Space Fortress). Activity patterns in the dorsal striatum were by far more predictive than average

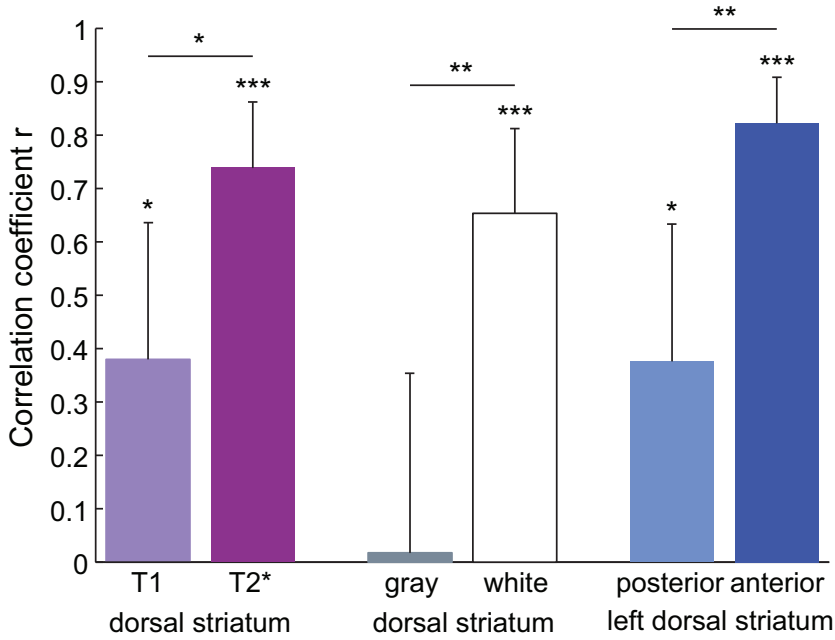

Figure 3.9: Comparison of prediction accuracy for various signal sources. Predictions based on patterns of T_1-weighted images (MPRAGE) in the dorsal striatum were significantly less accurate than those based on time-averaged T_2^*-weighted images (EPI). Voxels located in white matter allowed for much better predictions than those in gray matter within the dorsal striatum. Finally, decoding was significantly better from the anterior than the posterior half of the left dorsal striatum. Error bars indicate the 95% confidence interval for the Pearson correlation coefficients. $*p < 0.05, **p < 0.01, ***p < 0.001$.

activity levels (figures 3.4 and 3.6). Furthermore, activity patterns showed higher prediction accuracy in the left than in the right hemisphere (figure 3.7), and within the left hemisphere, the anterior half of the dorsal striatum was more predictive than its posterior half (figure 3.9).

The participation of the dorsal striatum in learning to play Space Fortress is consistent with its involvement in procedural and habit learning in the execution of learned behaviors (caudate nucleus) and motor learning (putamen) in non-human primates [16, 18, 19] and humans [4, 60, 61, 62]. Activity in the dorsal striatum has also been associated with tasks requiring cognitive flexibility [63] such as task-switching [20, 64] and transfer of training to untrained tasks [31, 32]. Being associated with reward and motivation, the nucleus accumbens in the ventral striatum has also been reported to participate in early stages of learning [24, 25, 26]. However,

we found patterns of time-averaged T_2^*-weighted signal in the nucleus accumbens not to be predictive of individual learning success.

Better performance in a video game has previously been related to an increase in dopamine release in both the dorsal and ventral striatum [27]. However, a study about the depletion of dopamine in rats [21, 64] suggested that the dopamine level in the caudate nucleus but not the nucleus accumbens was related to the initiation of complex goal-directed responses or performance, as measured by reaction time. In accordance with these reports we find that the time-averaged T_2^*-weighted signal in a region associated with learning new skills and procedures (caudate nucleus) is more predictive of learning success than the time-averaged T_2^*-weighted signal in sub-cortical regions associated with motor learning (putamen) or motivation and reinforcement (nucleus accumbens). As further evidence for this weighting of skills we find that improvement in the speed sub-score, which is related to speeded discrimination and working memory, is predicted much better by the time-averaged T_2^*-weighted signal in the dorsal striatum than improvement in the control and velocity sub-scores, which are related to motor control.

In a previous study Erickson et al. in [4] has demonstrated a link between the size of structures in the dorsal striatum and performance improvements by individual subjects. Here we show that patterns of pre-learning time-averaged T_2^*-weighted signal can explain as much as 68% of the variance among individuals (in the anterior half of the left dorsal striatum), while volumetric analysis based on automated segmentation of these anatomical regions could explain at most 23% of the variance. However, since the volumetric measurements in [4] and the time-averaged T_2^*-weighted patterns used in this work both measure aspects of the same region, the dorsal striatum, they may be related. Accordingly, a partial correlation analysis of score improvement predicted by time-averaged T_2^*-weighted activity versus measured score improvement showed almost no additional gain by introducing two additional explanatory variables, the volume of the dorsal striatum and initial game scores (table 3.1).

The ability to predict who will benefit the most from training has ramifications

beyond the realm of video games. Indeed, training on Space Fortress has been associated with enhanced flight control proficiency in novice pilots [65]. In many contexts, training can be prohibitively costly and time consuming, with high attrition rates (e.g., military pilots, air traffic controllers). Pre-training MRI scans could potentially mitigate such costs by predicting who will improve at a higher rate as a result of training or to identify groups of learners who might benefit from either extended programs of training or different types of training strategies. The superior prediction power of MVPA compared to behavioral tests may justify the additional cost of MRI scans. Of course, it might also be possible, in future studies, to uncover behavioral correlates of the MRI differences, which in turn could be used to predict learning of new skills. Furthermore, our technique of applying MVPA to the temporal mean of the time-averaged T_2^*-weighted EPI signal to predict individual differences in learning can be applied in other domains, possibly allowing for the understanding and prediction of learning as a function of development, aging, and neurodegenerative disorders. The fact that we use the gradient-echo EPI brain images, which are routinely used to measure functional activity, could make this new analysis technique especially attractive, because no new scans would need to be added to established experimental protocols. In fact, if successful in other learning contexts, the technique could be used to analyze existing data retrospectively.

Finally, the time-averaged T_2^* signal allowed for significantly more accurate predictions than the T_1 signal. This fact, along with the higher prediction rates for white than gray matter and being independent of the tasks at each block, suggests that individual differences among subjects may be due to differences in anatomical or persistent physiological features rather than differences in functional activation. The next chapter will discuss the follow-up study which includes more explicit measurements of tissue susceptibility such as susceptibility weighted imaging SWI as well as arterial spin labeling and diffusion tensor imaging in determining the exact nature of the signals that allow for such an accurate prediction of individuals' learning success.

CHAPTER 4

PHYSIOLOGICAL BASIS OF LEARNING PREDICTION IN TIME-AVERAGED T2*: NONHEME IRON

In spite of the astonishing accuracy (r = 0.74) of our predictions of the success of cognitive training in young adults as described in the previous chapter, the physical and physiological effects underlying this prediction are so far unclear. To explore this effect, we have conducted a new experiment, study 2010, in which we supplement the time series of T2*-weighted measurements (i.e. BOLD series) with T2-weighted, quantitative T2 (T2 map) and quantitative T2* (T2* map) measurements as well as susceptibility-weighted imaging (SWI), arterial spin labeling (ASL) and diffusion tensor imaging (DTI). Prediction accuracies of these different MR measurements indeed support a hypothesis that nonheme iron is a source for predicting learning in time-averaged T2*-weighted signal. This chapter describes this study in detail.

4.1 Follow-up experiment

4.1.1 Participants and training paradigms

Concerning non-imaging aspects, the design of this study was similar to that of the previous one. Particularly, all 48 recruited participants were young, right-handed adults between the ages of 18 and 30 with little video game experience (less than 5 hours per week) and no usage of cognitive-influencing medications. Among them, 45 completed the experiment, and of those, 6 were excluded from the analysis because of incomplete data acquisition. The final sample consisted of 39 young adult participants (mean age = 22, SD = 3.21, 12 males) with normal or corrected-to-normal visual acuity, normal color vision, and normal hearing. These participants were given two

scans in an MR session prior to the training period and an identical one after training; but again, only the scans from the first MR session are used to predict learning and study the mechanism(s) underlying the learning-predictive information discovered in the earlier study.

Nevertheless, the current study had its training regime modified based on experience with the previous study. The 2008 study had 10 two-hour training sessions, and participants were randomly assigned to practice with one of the two different training strategies (either fixed or variable priority). The learning curves of the trainees plateaued after about 10 hours of learning/practicing, and the variable priority training strategy was more effective than the fixed priority. Therefore, the current study included only 10 one-hour variable-priority training sessions. Each training session started with 1 warm-up trial and ended with 2 test-game ones (for performance measurement), during which participants were asked to maximize performance and focus on obtaining the highest total score by emphasizing each game component equally. Between the warm-up and test trials, there were five practice blocks, each consisting of three trials. During these training trials participants were asked to focus on improving and monitoring different aspects of the game (control, velocity, speed, points or total score).

4.1.2 Imaging design to discover learning-based information from time-averaged T2*-weighted signal

As the main motivation of this study was to examine the mechanisms underlying the prediction of learning and particularly the root of the learning-prediction information in the time-averaged T_2^*-weighted, the MR imaging sessions were designed to include many different imaging contrasts as well as quantitative measurements. Each MR session was run on a 3T Magnetom Trio (Siemens), and the following data sets were acquired:

- Arterial spin labeling (ASL): acquired by ASL-pTITL sequence [66]. The sequence were set with $TR = 5000$ms and $TE = 44$ms, included 30 averages

(actually it includes only 29 averages as it is recommended that the first pair of control/tagged images should be discarded) and collected 10 slices at 64×64 voxels. Each voxel was $3.4 \times 3.4 \times 4$mm (with a 20% of distance factor). In addition, overlays of T2-weighted images ($TR = 14$ms and $TE = 89$ms) were acquired with the same slice profile and having an in-slice resolution of 256×240 voxels/slice (voxel size is $1.7 \times 1.7 \times 4$mm and distance factor is 20%).

- Gradient-echo EPI BOLD (T2*-weighted) acquisition: there were 9 blocks of BOLD acquisition (gradient-echo EPI sequence) with $TR = 3000$ms, $TE = 25$ms and parallel imaging reduction factor of 2. Each block lasted 4 minutes, so a total of 80 volumes were collected during each block. Each volume had 50 slices and a 120 x 110 voxel matrix. The voxel size was $2.1333 \times 2.1333 \times 2.4000$mm.

  The 9 blocks consisted of two blocks of passively watching (PW: watching a sample video recording of the Space Fortress game played by an expert), two blocks of pure resting (PR: looking at a black screen background with a green object fixed at the center), three full of Space Fortress game playing (SF), one block of right-wrist left-finger motor localizer (rlML), and one of left-wrist right-finger motor localizer (lrML). In rlML, when the screen displayed "wrist" (W), the subjects moved the joystick with their right wrist; when it said "finger" (F), the subjects pressed the button with a left finger; and when it displayed "stop" (S), the subjects did not move their hand or wrist. The three conditions were arranged in the following order: SWSFSFSWSWSFSFSW. Similarly, for lrML, the subjects moved the joystick with their left wrist when they saw "wrist," pressed with their right finger when they saw "finger," and did not move their wrist or finger for "stop." Those tasks for lrML were arranged in the following order: SWSFSFSWSWSFSFSW. In general, the nine blocks were arranged in the following order: PW-PR-SF-SF-SF-PR-PW-rlML-lrML.

- High resolution T1-weighted: has $TR = 1900$ms and $TE = 2.26$ms. Acquire

$192 \times 232 \times 256$ voxels per volume. Each voxel is $1 \times 1 \times 1$mm.

- High resolution T2-weighted: $192 \times 240 \times 320$ voxels at $.8 \times .8 \times .8$mm. $TR = 2500$ms and $TE = 268$ms.

  In fact, instead of the two-dimensional sequences described in the section 2.4, for T_1- and T_2-weighted image acquisition, our study employed three-dimensional pulse magnetization-prepared 180-degree RF pulse and rapid gradient-echo (MPRAGE) [67] and T_2-weighted turbo-spin-echo (TSE) with high sampling efficiency (SPACE) [68] sequences, respectively. In a comparable acquisition time, these methods provide better contrast and truly three-dimensional reconstructed images.

- T2*-quantitative map (acquired with gradient-echo multi-contrast sequences gre-mc): 50 slices at 128×116 voxels and each voxel is $2.0 \times 2.0 \times 2.5$mm. $TR = 2450$ms. Totally twelve volumes are acquired at 12 different TE-values: 3.5, 5.97, 8.44, 10.91, 13.38, 15.85, 20, 25, 30, 35, 40, 46ms.

- T2-quantitative map (acquired with spin-echo multi-contrast sequences se-mc): include 36 slices, at 128×118 resolutions and each voxel is $2 \times 2 \times 3.6000$mm. TR value is 2850ms. Six volumes were acquired at different TE-values ($TE = 25, 50, 75, 100, 125, 150$ms).

  Note that in MR, *weighted* image and *map* (or quantitative) images are completely different. Particularly, for example, while in T2-weighted images, voxel intensity is mainly determined by T2-value and also slightly depends on other factors such as T1, proton density, etc.; in T2-map (after model fitting to find the map), voxel intensity supposedly reflects the true value of relaxation time T2.

- SWI: has $TR = 28$ms, $TE = 20$ms; include 72 slices at 448×350 voxels. Each voxel is $.7 \times .6 \times 1.7$mm. Besides SWI images, magnitude and phase images were saved.

- 30-direction DTI (with 2 averages): each volume has $128 \times 116 \times 50$ voxels and each voxel is $2.0 \times 2.0 \times 2.4$mm.

4.2 Principles and connections of the included imaging measurements

This section discusses the reasons for including the imaging sequences listed in the experiment design as well as their principles related to the pre-processing procedures applied before they enter the support vector predictor. These are important for explaining our hypothesis about the underlying physiological basis of the prediction power of time-averaged T_2^*-weighted signals.

4.2.1 T_1- and T_2-weighted images, T_2 and T_2^*-map

Originally T_1-weighted images were acquired to provide structural information of the participants' brains and as a control to verify the learning-predictive source of the time-averaged T_2^*. Given the direct relationship between T_2 and T_2^*, $\frac{1}{T_2^*} = \frac{1}{T_2} + \frac{1}{T_2'}$ (where T_2' or its equivalent relaxation rate R_2' is rooted from field inhomogeneity such as imperfect shimmed B_0 field or the local susceptibility of imaged objects), one pertinent test would be to see if T_2-weighted, rather than T_1-weighted, images would have the same predictive power. Note that there were not any T_2-weighted acquisition originally included in the Space Fortress 2008 study, so such a test could not be done before. In this follow-up study, which again includes T_1-weighted imaging, the T_2-weighted sequence was added.

During the preprocessing stage, T_1-weighted images were non-linearly registered to MNI, normalized and sub-sampled to $3.4375 \times 3.4375 \times 4$mm - all was similar to what was done in the previous study. T_2-weighted ones were non-linearly registered to MNI (by applying the non-linear wrapping of T_1-to-MNI registration and an affine transformation from T_2-to-T_1 of the same subject), as well as normalized and sub-sampled to the same resolution.

Although T_1- and T_2-weighted images can provide high-contrast structure information, quantitative measurement of these relaxations times even contains more information [69]. Therefore, we did include T_2-map (its equivalent is relaxation rate $R_2 = \frac{1}{T_2}$) and T_2^*-map (its equivalent is $R_2^* = \frac{1}{T_2^*}$) in study 2010. As mentioned in the experiment description, spin echo multi-contrast with 6 TEs and gradient echo multi-contrast with 12-TE sequences were used to measure the T_2- and T_2^*-maps, respectively. Note that it is crucial to acquire many more than two echos in an in-vivo experiment, as otherwise the unavoidable noise would make any quantitative map far from the true values [70]. From these scans, with a mono-exponential assumption [71, 72], we estimated the values of R_2 and R_2^*, and hence $R_2^{'}$ (or $R_2^{'} = \frac{1}{T_2^{'}} = R_2 + R_2^*$) as well. Although signal intensity decays exponentially, with a mono-exponential assumption, T_2 and T_2^* can be derived by solving least-square linear equations. Furthermore, in our experiment the first image in the series of 6 spin-echo images was a stimulated echo and hence was removed. It means that only 5 data points were used for the T_2 estimation.

Nevertheless, note that due to noise as well as partial volume effects, estimating T_2 and T_2^* quantitative maps with mono-exponential fits are prone to large error [70]. Indeed, besides the need of having many echoes acquired as well as taking into account the existence of many T_2 and T_2^* components, it was also necessary to repeat the measurements for signal averaging (to reduce noise). These tasks will be carried out in future work.

While T_1-weighted or map and T_2-weighted or map images are determined by the intrinsic longitudes T_1 and T_2 values, respectively, of the tissues (see section 2.4), it is important to note that these intrinsic relaxation times are not only governed by the amount of tissue water and the field strength B_0, but are also determined by the microscopic and macroscopic water distribution as well as its interaction with other macromolecules. In general, T_1 depends strongly on the magnetic field strength while T_2 does so only to some extent but is affected more strongly by water contents/distributions and their interactions with paramagnetic macromolecules such as iron-storage protein like ferritin.

Particularly, it is widely accepted that as water molecules diffuse through any microscopic field inhomogeneity (which can be caused by paramagnetic iron-containing molecules such as ferritin proteins or deoxygenated hemoglobin), the spins of the water protons experience dephasing during the time T_E, which cannot be reversed by spin echos. This loss of signal is technically equivalent to shortening T_2 (increasing R_2). This does not affect the T_1 value, as field inhomogeneity fluctuates slowly in comparison to $1/f_0$ (but rapidly in comparison to T_E) [73, 74, 58]. T_1, however, has its value shortened as a result of smaller magnetic ions coming into direct contact with water [75]. In fact, postmortem biochemical studies on patients with Alzheimer's disease, Parkinson's disease, and Huntington's disease showed that these patients had excessive amounts of brain iron in the basal ganglia, hippocampus and/or globus pallidus and they are in agreement with MR studies reporting significant shortening of the T_2-values in these regions of those patients [76, 77, 78, 79].

Besides, T_2 also depends on the water content; i.e., the more water, the more the relaxation rate of R_2 decreases (T_2 increases) [80, 73, 74, 58]. In short, up to now, the models that regulate T_1 and T_2 relaxation rate in MR measurement are not clearly explained in theory, and so we cannot yet calculate T_1, T_2-values theoretically, nor can their quantitative measurement be used to quantify paramagnetic substances such as iron-carrying proteins.

4.2.2 Susceptibility-weighted imaging

As susceptibility or field variation leads to the relaxation time T_2^* instead of T_2, it is desirable to measure the susceptibility as well as crucial to understand its physiological sources. Therefore, we included a susceptibility-weighted imaging SWI sequence [6, 81, 7] in this new experiment.

Principles

In MR imaging, collected raw k-space data consist of both magnitude and phase information; however, since most MR applications only aim to get the magnitude image information, while discarding the phase information. Indeed, besides including phase-encoding spatial information (see section 2.4), phase images also contain undesired background phase data resulting from global geometry distortions, and useful local phase variations rooted in paramagnetic iron compounds such as deoxygenated hemoglobin or ferritin protein in the brain. Susceptibility-weighted imaging (SWI) has emerged as an imaging technique utilizing phase information related to local *magnetic susceptibility variation* in tissues. At each voxel, the spectral information from the tissues that had distinct magnetic susceptibility differences relative to their surroundings, such as iron-containing tissues or deoxygenated-blood ones, was extracted from the SWI phase map (assuming no chemical shifts).

Specifically, magnetic susceptibility is defined as a proportionality constant relating to the induced magnetism of a material in response to an applied magnetic field. Denoting M as the induced magnetization when an object is placed inside a uniform magnetic field, we have $M = \chi B/\mu_0/(1+\chi) = \chi B/\mu_0$ (assume $\chi << 1$), where μ_0 is the permeability in a vacuum, and $\chi = \mu_r - 1$ is the magnetic susceptibility (μ_r is the relative permeability). In return, this induced magnetization causes distortion to the uniform external field. Therefore, for adjacent objects with difference magnetic susceptibility, local field variations ΔB occur around and within them.

Recall that if we assume complete homogeneity of the B_0 field, A_E, the signal intensity response from the α-degree gradient-echo sequence will be as in equation 2.7. However, if there are local field deviations, the collected signals will be $A = A_E e^{-i\gamma\Delta B T_E}$. In other words, local field differences lead to variations in the phases of collected MR signals $\varphi = -\gamma\Delta B T_E$. Phase variation is contributed by several different field variations:

$$\varphi = -\gamma\left(\Delta B_{\text{local geometry}} + \Delta B_{\text{cs}} + \Delta B_{\text{global geometry}} + \Delta B_{\text{main field}}\right) T_E$$

where $\Delta B_{\text{local geometry}}$ is the microscopic field variation caused by, for example, changes in the amounts of local iron content (spins in tissues loaded with paramagnetic iron elements align along the $\vec{B_0}$ direction and thus make the local field larger than its background); B_{cs} represents field changes due to chemical shift; and $\Delta B_{\text{global geometry}}$ and $\Delta B_{\text{main field}}$ are macroscopic ones that result from object geometry (such as the air/tissue interface at the frontal region of the brain) and the inhomogeneity of B_0, respectively. The two macroscopic field variations have low spatial frequency in general. Indeed they lead to artifacts and are subjected to elimination by a high-pass filter for our purpose [82].

Particularly, neglecting the field changes due to chemical shift, denote $I_0(x)$ as the original complex signal including the phase variations due to field inhomogeneity and global geometry $\varphi_f(x)$ as well as the microscopic ones $\varphi_v(x)$:

$$I_0(x) = |I_0(x)|e^{i\varphi_f(x)+i\varphi_v(x)} = F^{-1}\left[S(k)\right]$$

where $S(k)$ is the collected k-space data from the scanner. Next, a low-pass filter $H(k)$ is applied to get image $I_h(x)$

$$I_h(x) = |I_h(x)|e^{i\varphi_f(x)} = F^{-1}\left[S(k)H(k)\right]$$

Finally, a high-pass filtered image, $I_f(x)$, can be obtained through:

$$I_f(x) = \frac{|I_0(x)|e^{i\varphi_f(x)+i\varphi_v(x)}}{|I_h(x)|e^{i\varphi_f(x)}} = |I_f(x)|e^{i\varphi_v(x)}$$

In practice, a Hanning low-pass k-space filter of the size 64×64 or smaller can remove most of the undesired macroscopic field without losing much of the phase contrasts of the structures of interest.

In short, with the assumption of no chemical shift and the application of a high-pass filter, the microscopic phase information $\varphi_v(x)$ can be determined, and so can the microscopic field variation $\Delta B_{\text{local geometry}} = \frac{\varphi_v}{-\gamma T_E}$ – which is considered as proportional to iron-concentration [83].

Heme and nonheme iron

The phase obtained above stems from two different sources: heme and nonheme iron.

- Heme iron: This kind of iron is found in blood hemoglobin and some enzymes like peroxidases. The iron in hemoglobin is crucial for transporting oxygen from the lungs to the tissues. Deoxygenated hemoglobin molecules are paramagnetic (the difference in susceptibility between deoxygenated hemoglobin and the surrounding tissue is about 1.5ppm [74]), but when oxygen molecules bind to it, the net spin becomes zero and it is technically diamagnetic. In fact, the root of BOLD contrast is the change of hemoglobin from oxygenated and diamagnetic to deoxygenated and paramagnetic.

- Nonheme iron: Nonhemoglobin iron is present mostly in iron-storage proteins (ferritin and hemosiderin) and iron-transporting transferrin. Although the total amount of iron in an average 70kg body is only about 3700mg, of which about 2500mg is heme iron and 1000mg is in iron-storage proteins, thanks to its uneven distribution, its susceptibility is about $1 - 10$ppm more positive than the surrounding iron-free tissues. Indeed it is concentrated only in certain tissues: most iron-storage proteins in the brain are found in the globus pallidus, substantia nigra, putamen, caudate and hippocampus. The concentrations in the basal ganglia are the highest, a few times higher $(2 - 4)$ than those in the cortical regions. Moreover, only iron in iron-storage proteins is the nonheme iron which can produce detectable MR contrasts, due to the fact that there are thousands of iron atoms within each of their molecules (as compared to two iron atoms bound in transferrin), and in the brain their concentration is more than 10 times that of transferrin [74, 58].

  Brain nonheme iron concentrations increase quickly during the first 20 years, slow down after that and become steady in the midlife of healthy adults [84]. Its important role in learning has been shown in many studies on both (iron-deficient) animal and human [41, 9, 10, 85, 11]. Possible mediating mechanisms of nonheme iron on learning include its effects on functioning and

metabolism of dopamine [35, 36, 37, 86, 87], hippocampus integrity [39, 40, 41] and myelination regulation [42].

Note that in MR, other forms of nonheme iron including ionic iron, low-molecular-weight complexes, and other metaloproteins such as melanotransferrin and lactoferrin, as well as other ferromagnetic molecules such as those containing copper or manganese, are ignored because their amounts are often too small to alter MR contrasts. And also note that in the phase information described above, the iron content includes both heme and nonheme iron [58].

Furthermore, as mentioned in the previous section, an induced magnetic field surrounding iron-storage proteins like ferritin and hemosiderin leads to the dephasing of water spins as the water diffuses in the affected area; and as the applied field strength increases, magnetization of paramagnetic particles increases, R_2 experiences a larger increase (equivalent to hypointensity or dark areas in T_2 images) [75, 88]. However, as there are other factors affecting R_2 such as water content, it is not reliable to try to measure iron concentrations with R_2 measurements. In fact, not all areas that have large R_2 have high iron concentrations (such as the low-T_2 yet iron-free ocular lens).

4.2.3 Diffusion tensor imaging DTI

While in our previous study, we found that time-averaged T_2^*-weighted signal at white matter area has more predictive information than at gray matter, water diffuses in white matter with mostly fibrous components in a more anisotropic fashion than in gray matter. Indeed, this anisotropy information can be well characterized with diffusion tensor imaging measurements; i.e., microscopic structures can be captured via water diffusion information. So in the quest to find the physiological source of predictive information, DTI data collection is of interest.

Principles

Water molecules in tissue move randomly and, depending on the surrounding structures, they can bounce off, go through, or interact with tissue components. This is known as water diffusion, with the appropriate gradient pulse application, MR can capture this diffusion information. In particular, an MR diffusion-weighted image can be obtained by applying two opposite gradient pulses (or two identical ones with a 180^0 pulse in the middle) after excitation and before the acquisition pulses. With the first gradient application, depending on their positions along the gradient direction, the spins will dephase differently. This dephasing effect will be completely reversed due to the application of the opposite polarity but will have an identical shape if the molecules have been still. However, if in the duration between the two gradient applications, the molecules have diffused along the gradient direction, the spins cannot rephase completely, resulting in an attenuation of the collected signal in the corresponding areas of molecular diffusion.

$$A = e^{-bD}$$

where D is the diffusion coefficient along the gradient direction and b (called the b-factor) depends on the shape, amplitude and timing of the gradient pulses.

In fact, due to their thermal energy, water molecules in tissue move randomly in three dimensions. Hence, displacement of the molecules during diffusion fully reflects the underlying structures and geometric organization of the tissue at the microscopic level. For example, due to the orientation of neuronal fibers, water molecules in white matter diffuse anisotropically, i.e. easily along neuronal directions and more restrictedly in perpendicular ones. So, to characterize molecular mobility and its correlations in all three dimensions, the diffusion tensor $\underline{D}$ [89] is defined as follows:

$$\underline{D} = \begin{pmatrix} D_{xx} & D_{xy} & D_{xz} \\ D_{yx} & D_{yy} & D_{yz} \\ D_{zx} & D_{zy} & D_{zz} \end{pmatrix}$$

where D_{ii} reflects molecular displacement along the dimension i and $D_{ij} = D_{ji}$ shows the correlation of the molecular motilities along directions i and j (with $i, j = x, y, z$). Also, the b-factor is now a $\underline{b}$ matrix and the attenuation of the collected signal becomes the following:

$$A = e^{\left(-\sum_{i=x,y,z}\sum_{j=x,y,z} b_{ij}D_{ij}\right)} = e^{-D_{xx}-D_{yy}-D_{zz}-2D_{xy}-2D_{xz}-2D_{zy}}$$

In principle, for each voxel, at least six measurements are required to derive the diffusion tensor. In practice, it is better to choose the same b-value for all gradient directions, and the gradient directions should ensure uniformity of the sampling. Furthermore, to improve SNR, the set of measurements is usually repeated for averaging. Also, to calculate the attenuation ratio A, it is necessary to acquire an image with no diffusion ($b = 0$).

$\underline{D}$ can be calculated for each voxel from the set of diffusion-weighted images. To find the three main directions of diffusivity, eigenvectors x', y', z' and their corresponding eigenvalues $(\lambda_1, \lambda_2, \lambda_3)$ of $\underline{D}$ are calculated. Furthermore, to represent the 3-D area encompassing the diffusion distance of the molecules in a voxel during diffusion time T_d, a diffusion ellipsoid for each voxel is proposed: $x'^2/(2\lambda_1 T_d) + y'^2/(2\lambda_2 T_d) + z'^2/(2\lambda_3 T_d) = 1$. The three main axes of the ellipsoid are the three main diffusion directions, and its eccentricity describes the anisotropy level of the diffusion. The term λ_1 is sometimes referred to as the axial or parallel diffusivity ($\lambda_{||}$) in the sense that it represents the diffusivity along the principal axis. The diffusivities in the two minor directions are usually represented by the radial diffusivity $(\lambda_2 + \lambda_3)/2$. In addition, the overall diffusivity within a voxel is usually described by an invariant (reference-frame-independent) measurement called the Trace: $Tr(\underline{D}) = D_{xx} + D_{yy} + D_{zz} = \lambda_1 + \lambda_2 + \lambda_3$. The mean diffusivity is equal to $Tr(\underline{D})/3$. The mean diffusivity decreases with gliosis and increases with extracellular fluid accumulation [90].

For the relative degree of the diffusion anisotropy in a voxel, the following invariant indices are also used [91]:

- Relative anisotropy RA: ratio of anisotropic part of $\underline{D}$ to its isotropic one. Ranging from 0 (isotropic or spherical) to $\sqrt{2}$.

$$\begin{aligned} RA &= \frac{\sqrt{\left(\lambda_1-\bar{\lambda}\right)^2+\left(\lambda_2-\bar{\lambda}\right)^2+\left(\lambda_3-\bar{\lambda}\right)^2}}{\sqrt{3\bar{\lambda}}} \\ &= \frac{\sqrt{\left(\lambda_1-\lambda_2\right)^2+\left(\lambda_1-\lambda_3\right)^2+\left(\lambda_2-\lambda_3\right)^2}}{\sqrt{\bar{\lambda}}} \end{aligned}$$

  where $\bar{\lambda}=\dfrac{\lambda_1+\lambda_2+\lambda_3}{3}$

- Fractional anisotropy FA: portion of anisotropy in total "magnitude" of $\underline{D}$. Ranging from 0 (isotropic) to 1. Indeed, it is related to the degree of coherence of the fiber tract. In particular, where fiber bundles merge, fractional anisotropy decreases [92].

$$\begin{aligned} FA &= \frac{\sqrt{3\left(\lambda_1-\bar{\lambda}\right)^2+\left(\lambda_2-\bar{\lambda}\right)^2+\left(\lambda_3-\bar{\lambda}\right)^2}}{\sqrt{2\left(\lambda_1^2+\lambda_2^2+\lambda_3^2\right)}} \\ &= \frac{\sqrt{\left(\lambda_1-\lambda_2\right)^2+\left(\lambda_1-\lambda_3\right)^2+\left(\lambda_2-\lambda_3\right)^2}}{\sqrt{2\left(\lambda_1^2+\lambda_2^2+\lambda_3^2\right)}} \end{aligned}$$

- Volume ratio VR: ratio of volume of ellipsoid over sphere of radius $\bar{\lambda}$. Ranging from 1 (isotropic) to 0.

$$VR=\frac{\lambda_1\lambda_2\lambda_3}{\bar{\lambda}^3}$$

4.2.4 Perfusion-weighted imaging - arterial spin labeling

In our original study, while the subjects were doing different cognitive tasks inside the magnet, including playing the game, we used a gradient-echo EPI sequence to acquire a time series of BOLD images, in which contrasts come from the paramagnetic and diamagnetic properties of de-oxygenated and oxygenated hemoglobin, respectively. Therefore, it is possible that predictive information within its time-averaged signal might rise with the amount of blood perfusing into the regions. To verify this

possibility, in this new study, we included explicit measurements of blood perfusion with the pseudo-continuous transfer-insensitive labeling technique (pTILT) ASL sequence [66].

Principles

Instead of measuring blood perfusion with the use of an exogenous tracer (i.e. the injection of a contrast agent into the blood stream), the non-invasive perfusion measurement with arterial spin labeling of MR utilizes an RF pulse to "label" or "tag" water protons. Water spins in the blood stream are *inverted* (inversion pulse) or *nulled* (saturation pulse) (hence the terms "tagged") when traveling in the arterial tree and before flowing into the brain, i.e. around the neck area. One to two seconds after tagging, the tagged blood reaches the targeted imaging area. The amount of signal it contributes to the total signal is certainly different from when there is no tagging. A few seconds after acquiring the tagged image, a non-tagged image, the control image, can be collected from the exact same region (by this time, the tracer-effect of labeled water-protons has decayed completely due to longitudinal relaxation T_1). Hence, if it is assumed that the signal change is only due to perfusion effects (of tagged and non-tagged blood), perfusion information can be obtained.

Basically, there are two types of ASL: continuous ASL (CASL) (continuously labeling blood water protons) and pulsed one (PASL) (using a short RF pulse to invert a slab of arterial blood). In general, PASL has a lower signal-to-noise ratio than CASL [93]. Over the years the two techniques have been improved with many modified versions. In our study, we used the pseudo-continuous transfer insensitive labeling technique (pTILT) sequence [66] which retains the magnetization transfer-insensitive properties like PASL but realizes pseudo-continuous tagging with non-adiabatic pulses similar to CASL. However, like other blood water labeling techniques, the contrast-to-noise ratio (CNR) of this method is very low (in general, the CNR of ASL is lower than BOLD by a factor of 2 to 4). In our study, we took 29 averages to enhance the CNR of the ASL signal. Furthermore, as a result of T_1-decay of the

tagged spins, all data acquisition has to be completed in a short time window, so there are usually only a certain number of slices that can be acquired. In our study, we acquired a total of 10 slices, always adjusting the field of view so that it covered the basal ganglia of each subject. Note that, as the in-plane resolution of ASL is also not very high, besides the pTILT acquisition, T_2-weighted images of overlying structures were also acquired.

Ideally, perfusion can be derived from the subtraction signal with the following equation:

$$CBF = \frac{\Delta M}{M_{0,\mathrm{CSF}}} \frac{6000}{2\lambda_{\mathrm{blood}} \alpha T_{1,\mathrm{blood}}} e^{\left(\frac{\omega + T_{\mathrm{slc}}(n-1)}{T_{1,\mathrm{blood}}}\right)} e^{\left(\frac{T_E}{T_{2,\mathrm{blood}}}\right)}$$

where ΔM: flow-weighted image (the result of subtracting the control image from the tagged one); $M_{0,\mathrm{CSF}}$: measured intensity of cerebrospinal fluid (CSF) in a voxel in the ventricles; λ_{blood}: water content of blood (0.76). α: labeling efficiency; ω: post-labeling delay; $T_{1,\mathrm{blood}}$: longitudinal relaxation rate of blood (1680ms at 3 T). $T_{2,\mathrm{blood}}$: transversal relaxation rate of blood (275 ms at 3 T); T_{slc}: EPI readout duration of a single slice; and n: index of acquired slice [66].

The subtraction image should not be negative at any place: it is zero in regions with no perfusion and positive elsewhere. In fact, inaccurate values are often seen in ASL measurements, due to factors such as macrovascular signal inclusion, arrival-time delay, finite bolus width, BOLD contamination, etc.

4.3 Results

4.3.1 Effect of averaging time series of T2*-weighted images

Recall that besides carrying T_2 decay information which is influenced by paramagnetic substance such as iron storage protein in the brain (see section 4.2.1), T_2^*-weighted signals bear an additional signal loss due to field variation (characterized by the relaxation-time constant $R_2^{'}$). Ignoring chemical shift, as well as macroscopic field inhomogeneity (as in the case of good shimming), T2*-weighted signals are affected

by the susceptibility of heme and nonheme iron substance. In BOLD applications, time variation in T2*-weighted signals is associated with changes in the amount of oxygenated hemoglobin in the activated region [5], while in some other application such as [94, 8], T_2^* has also been investigated as a tool to evaluate iron content.

Furthermore, gradient-echo T_2^*-weighted images experience some complications in signal loss. Particularly, it might bear a non-exponential decay and depend on both the imaging gradient and voxel sizes (in comparison to the sizes of the structures causing field inhomogeneity within it) [95]. Due to its sensitivity to any magnetic variation, including one that is uncorrelated to the local susceptibility of the iron substance, T_2^*-images also suffer signal losses not related to tissue iron concentration.

In signal processing, to increase signal strength relative to noise, researchers commonly use time-averaging. Particularly, let us denote by S a signal strength that is constant in replicate measurements and by σ the standard deviation of the noise N (N varies randomly in repeated measurements). Under the assumptions of no correlation between signal and noise, and constant variance, after n measurements, the sum of the signal is nS, and the variance of the sum of the noise will be $n\sigma^2$. Thus, the signal to noise ratio (SNR) is:

$$SNR = \frac{nS}{\sqrt{n\sigma^2}} = \sqrt{n}\frac{S}{\sigma}$$

So averaging the signal improves SNR by the square root of the number of repeated measurements.

As mentioned above, in our study the voxel intensity in each image of the T2*-weighted time series was governed by time-invariant components such as $T2$, nonheme iron concentration, and time fluctuating factors such as heme iron (in blood) and noise. By averaging hundreds of them in the time domain, we improved the strength of the steady parts over the time-varying components (either in a stimulus-unrelated fashion like random noise, or stimulus-induced responses of blood/hemoglobin) by a factor of $\sqrt{n}$. In the case of the previous study, averaging was done over all 7 blocks (120 volumes in each block). In the current one, it was 9 blocks

(80 volumes in each block). Improvement factors of $\sqrt{120 \times 7} = 28.98$ and $\sqrt{80 \times 9} = 26.83$, respectively, were gained. So the predictive information that we have seen from T2*-weighted is likely from the time-invariant physiology components such as nonheme iron concentration and T2-value, and not from the heme iron concentration in blood.

This hypothesis is indeed supported by the fact that despite the types of stimulus during which we collected time series of T2*-weighted images in both studies, similar prediction accuracies were obtained.

Furthermore, in study 2010, when we use perfusion information (which should directly relate to the amount of heme-iron in the blood) obtained by a pTILT-ASL sequence, support vector regression cannot pick up the information related to the participant's learning.

At this point, it should be noted that there is a close connection between the two time-invariant components: nonheme-iron concentration and T2, especially in the basal ganglia where most brain storage-iron is found. That is, T2 of water protons is actually shortened by nearby paramagnetic-iron substances (see section 4.2.1 for more details) while effects of other paramagnetic substances in the brain on T2 are often neglected due to their tiny concentrations. In fact, people do take advantage of iron-induced T2-shortening to assess iron content in the brain
[96, 58, 97, 98, 74, 75, 88].

We would like to test our hypothesis with the data sets collected in study 2010.

4.3.2 Comparing prediction power of time-averaged T2*-weighted in the 2010 study to the 2008

As an important validation for the existence of learning-prediction information in the time-averaged T2*-weighted signal, we compared the analyses of the time-averaged T2*-weighted signals from 2008 to the corresponding data sets in the 2010 study.

From figure 4.1, we can see that there is, again, no learning-prediction information in the time-averaged T2*-weighted signal at ventral striatum (i.e. nucleus accumbens)

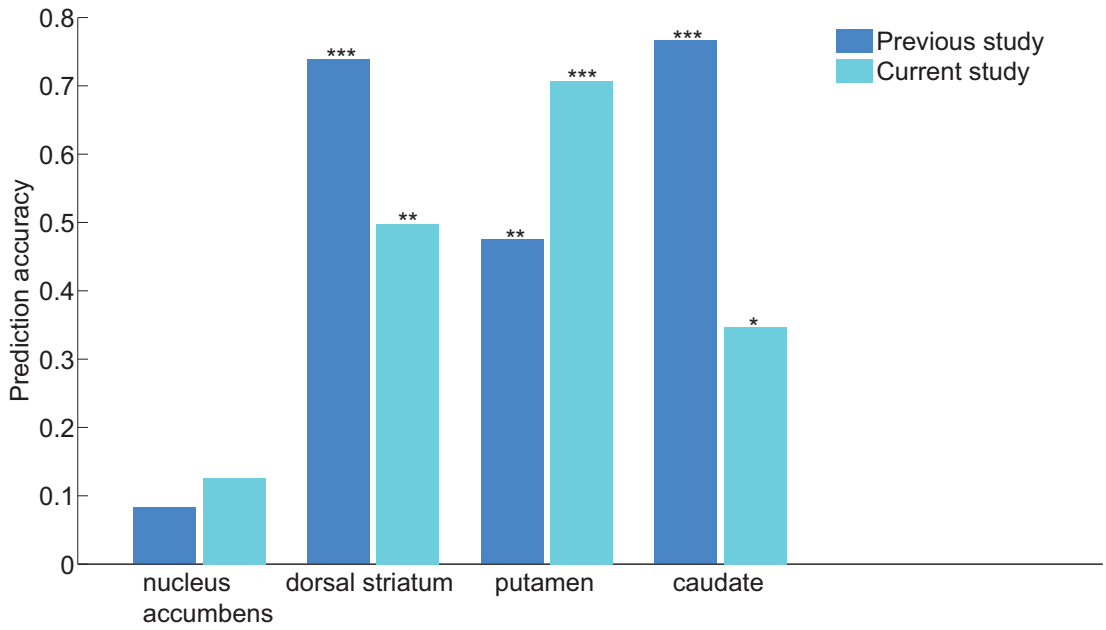

Figure 4.1: Comparison of prediction accuracy of time-averaged T2* signal in the previous and current study.

(r was $.1258$ and not significant in 2010, whereas r was $.0836$ and not significant in 2008) while the pattern of the time-averaged signal at the dorsal striatum repeats its predictive performance at a significant level (r in 2010 study was $.498$, $p < .01$, whereas r in 2008 was $.74$, $p < .001$). In other words, the relationship between the predictive information in the time-averaged T2* signals at the dorsal and ventral striatum remains unchanged, and once more *the role in learning of the dorsal striatum, not the dorsal striatum*, is confirmed.

While the prediction accuracy of the time-averaged T2*-weighted from putamen was $r = .47$ ($p < .01$) for the 2008 study and $r = .71$ ($p < .001$) for 2010 (they both are significant), prediction accuracy from caudate nucleus was $r = .77$ ($p < .001$) in study 2008 and $r = .38$ ($p < .05$, still significant) in the new study. At first this seems against our hypothesis that the learning predictive information is from the time-invariant brain nonheme iron; i.e., if the hypothesis holds, there should not be significant difference in prediction performance of time-averaged T2* signal in the two studies. However, as we checked the settings of our T2*-weighted acquisition, we discovered that parallel imaging was turned off in study 2008, but was on in study

2010. Parallel imaging, in principle, reduces susceptibility contrast/effects (including the ones caused by paramagnetic substances, for example, ferritin) [99]. So the drops in prediction accuracy of time-averaged T2* signal from caudate in study 2010 are indeed consistent with our hypothesis.

4.3.3 Mean diffusivity and learning-prediction

Recall that DTI data collection is comprised of many DWI acquisitions (see section 4.2.3) and actually they are widely used as markers in aging studies which have confirmed the relation between iron accumulation in deep gray matter and age [100, 101, 102]. These applications of DTI and DWI based on signal loss (hypointensity in the collected images) due to the iron content of the associated regions, i.e. DTI measurements, are affected by nonheme iron deposits. Indeed, a recent study by [103] has shown the agreement, and hence connection, between DTI data and nonheme iron concentrations in the brain in the deep gray matter (where the iron concentration is largest and sufficient to result in the dephasing of enough water spins to be detectable by MR). In that study, iron content was measured by fast spin-echo at two different field strengths, 1.5T and 3.0T, based on the field-dependent relaxation rate FDRI method [104, 101, 102]. More particularly the putamen and caudate nucleus structures, in which iron is deposited and accumulates with age, of the older group have higher anisotropy and diffusivity than those of the younger group. Although the mechanism has not yet been understood, the study also finds that in the white matter area, the older group has lower anisotropy (while the diffusivity is still higher) than the younger cohort; i.e., the increase of anisotropy with iron concentration in the deep gray matter regions might relate to microstructural alterations of tissues.

In short, both mean diffusivity and time-averaged T2*-weighted signal are related to brain nonheme iron in the deep gray matter. And indeed, as shown in figure 4.2, across the regions of interest, their learning predictions seem related. Hence, the role of the common factor, nonheme iron, in learning seemed to be confirmed by these interrelations.

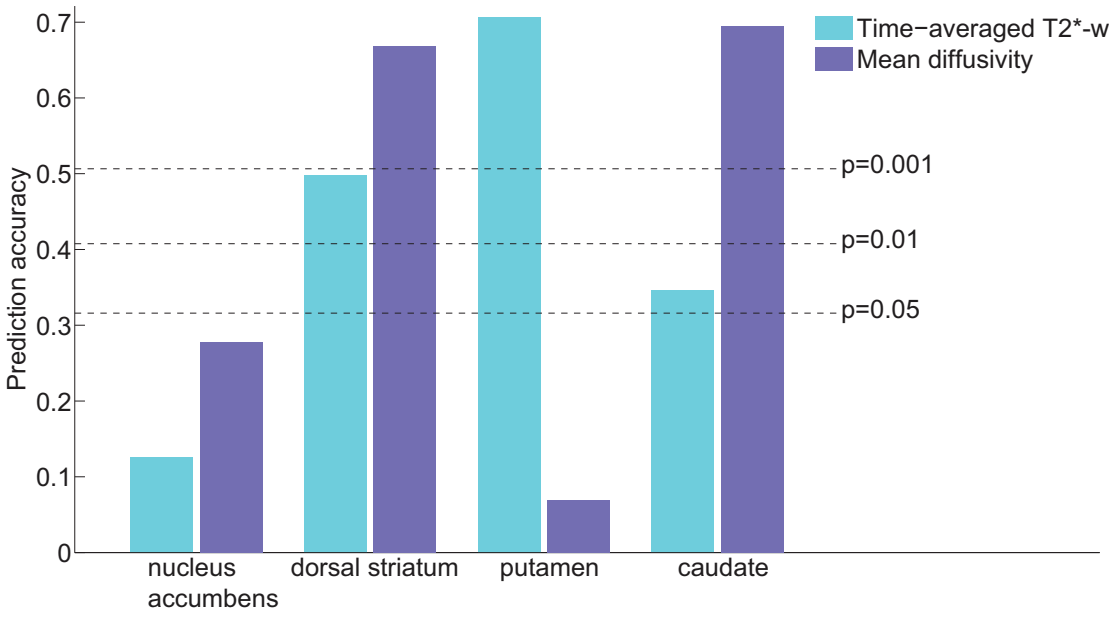

Figure 4.2: Predictive information in mean diffusivity.

Additionally, a comparison again shows mean diffusivity in the dorsal striatum predicting learning success with a significantly higher accuracy than the same measurement in the ventral striatum, $r = .69$, $p = 3.4 \times 10^{-}6$ vs. $r = .28$, $p = .09$ (not significant).

4.3.4 Learning prediction accuracies of T2- and T1-weighted images

Figure 4.3 also shows the significant accuracy of prediction from T1-weighted and T2-weighted at dorsal striatum, and not ventral; it also compares prediction accuracy obtained with input of predictors from T1-weighted and T2-weighted images. Particularly, for caudate, the prediction accuracy of the T2-weighted data is almost significantly higher ($p = .0632$) than that of the T1-weighted. This is in-line with the fact that the shortening effect of iron on the relaxation times is more prominent on T2-values and less so on T1 [80, 73] (details in section 4.2.1); i.e., in a sense, iron-concentration are reflected better by $T2$-values than $T1$-values. In short, it reaffirms the role of the underlying nonheme iron in the possibility of predicting learning of time-averaged T2-weighted images.

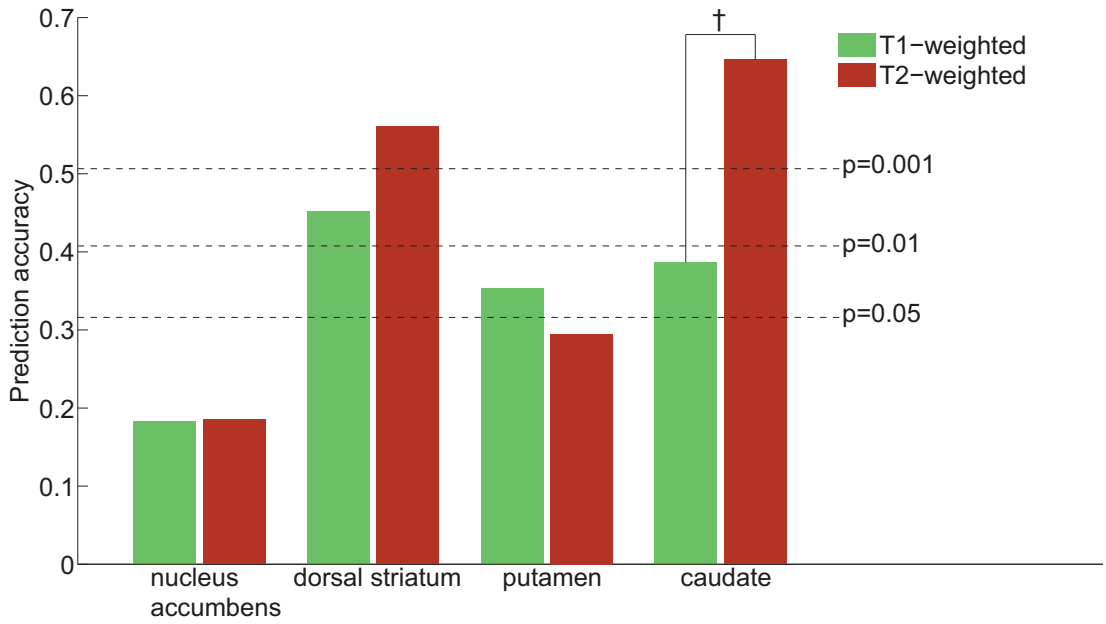

Figure 4.3: Prediction accuracy of information in T1-weighted and T2-weighted images. $\dagger p = .06319$.

4.3.5 Prediction from SWI vs. time-averaged T2*-weighted imaging

As figure 4.4 shows, in general, the microscopic phase responses extracted from SWI acquisition do not significantly predict learning improvement and their accuracy is lower than that of time-averaged T2*-weighted images. However, over the twelve regions on which we do our analysis, they perform very similarly to the time-averaged T2*-weighted signals. The correlation between the two curves in figure 4.4 is .65 (p=.0211).

From the explanation of SWI's microscopic phase extracting procedure as well as the explanation of SWI's sensitivity in section 4.2.2, it is clear that SWI contains both heme and nonheme iron content. Therefore, these prediction accuracies of SWI indeed further confirm the unrelated-nature of heme iron (supported by the fact that SWI's prediction accuracy is lower than time-averaged T2*-weighted), and they confirm the role of nonheme iron concentration in time-averaged T2*-weighted signals in learning prediction (supported by the similarity in prediction accuracies of SWI and time-averaged T2*-weighted).

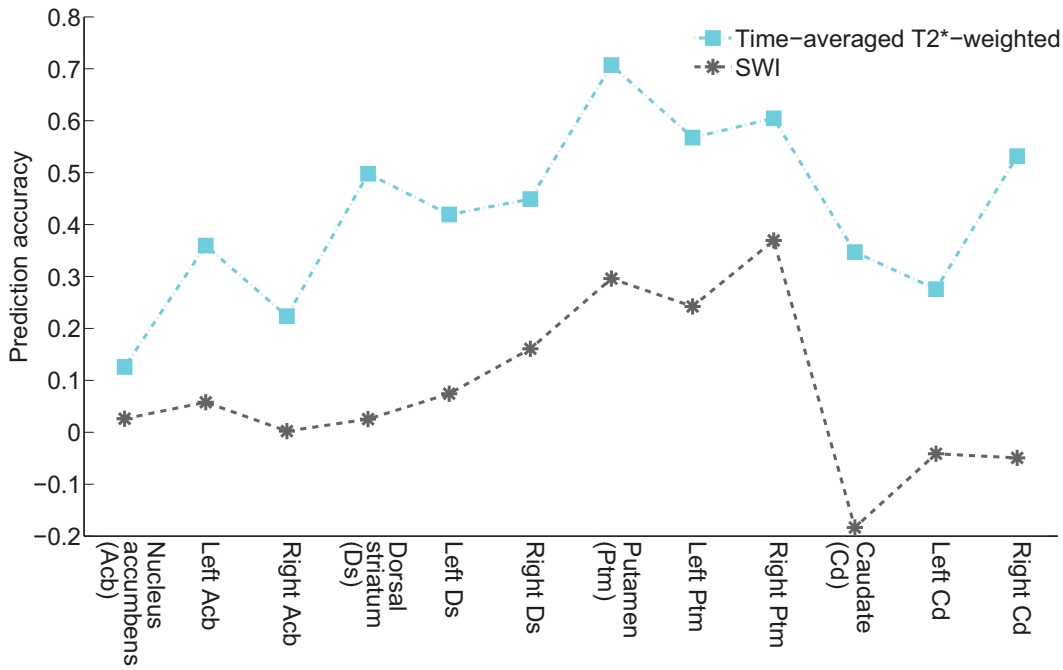

Figure 4.4: Prediction accuracy of time-averaged T2*-weighted and susceptibility-weighted imaging.

4.3.6 Prediction from R2 and R2' at ventral and dorsal striatum

We further verify our hypothesis with the behavior of predictive information in R_2 ($R_2 = \frac{1}{T_2}$) and R_2 ($R_2 = \frac{1}{R_2}$). In figure 4.5, like the time-averaged T2*-weighted signal, R2'-map has a significant prediction accuracy ($r = .4.339$, $p = .0058$) in the dorsal striatum, and no predictive accuracy in the ventral striatum, while there is no significant predictive information from R2 in either the dorsal or ventral striatum. Nevertheless, information in the R2-maps does demonstrate that the dorsal striatum has more predictive information than the ventral striatum.

At this point, it is important to note that R2' is considered to reveal the iron concentration better than R2. It is because, although R2 increases in areas that have high iron concentrations such as the deep gray matter, they do decrease as water content increases (gray matter has more water than white matter [105]). R2' on the other hand is only related to signal loss due to field variation, so it has more information relevant to iron content. This was discussed in more detail in sections 4.2.1 and 4.2.2.

The prediction accuracy from R2' (and R2) is not high in general is in-line with our hypothesis that only nonheme iron serves in learning prediction as R2' is influenced by both heme and nonheme iron.

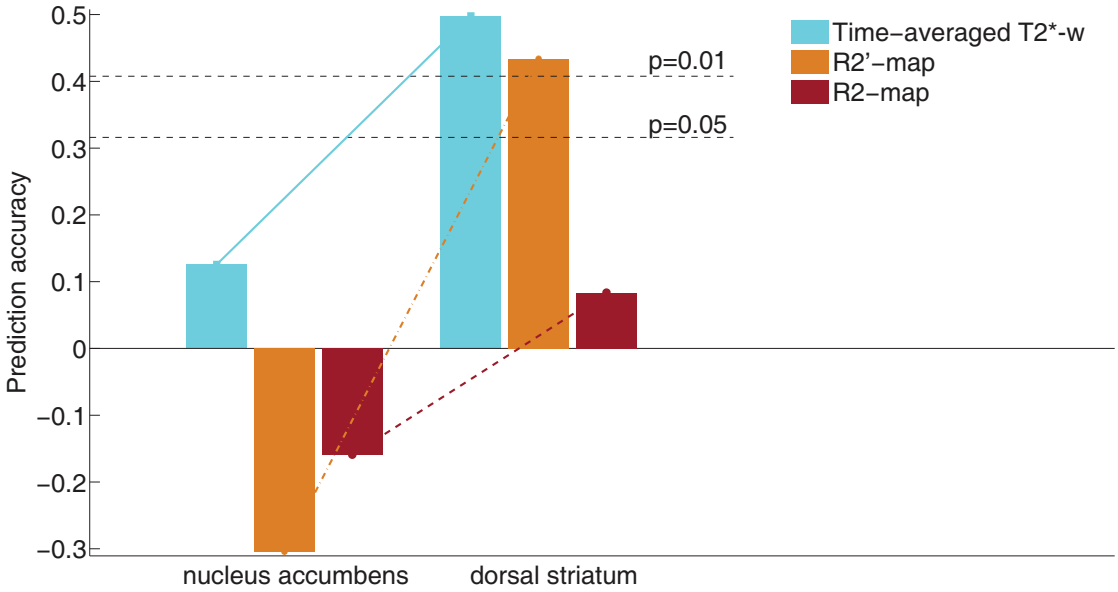

Figure 4.5: Prediction accuracy of R2-maps and R2' maps (in comparison to time-averaged T2*-weighted image) of ventral vs. dorsal striata.

4.3.7 Iron and learning

Although we conducted our studies and established our hypothesis completely based on the analysis results, our hypothesis is consistent with a vast literature in neuroscience about the crucial role of nonheme iron in learning. Particularly, non-imaging (and usually highly invasive) studies have also confirmed the roles of brain (nonheme) iron in learning based on animal models [41, 9] or on iron-deficient human populations [10, 85]. Nevertheless, the mechanism of the role of brain iron in learning is not yet fully understood. The three main possible explanations for the effect of iron on learning are via effects of iron on metabolism and the function of dopamine [35, 36, 37, 38], hippocampus structure and function [39, 40, 41], and degree of myelination [42].

Our regions of interests, the caudate nucleus, putamen and nucleus accumbens, have

particularly high concentrations of dopamine [27, 21, 64] and iron; note that there is a colocalization (distributed in the same area) in the brain between iron and dopamine [33, 34]. While dopamine plays an important role in learning [27, 28, 29, 30], dopamine function and metabolism are altered by iron [35, 36, 37, 38, 9]. Particularly, Yehuda et al. [9] showed that iron-deficient rats had learning deficits related to decreased functional activity of the dopaminergic neurotransmissions (even prior to hemoglobin reduction). Reduction in dopamine reuptake was also shown in iron-deficient anemic rats [37]. Furthermore, iron overload does have toxic effects on dopaminergic neurons and concentrations [106, 107]. See [11] for a thorough review regarding the role of iron in learning and memory.

CHAPTER 5

FUTURE DIRECTIONS AND CONCLUSIONS

5.1 Future directions

Understanding the effect of brain iron concentration and distribution on learning and memory of young healthy adults is important as it can provide crucial information for the design of assessments as well as interventions to improve these abilities.

For healthy older adults, on one hand, it has also been shown that more iron accumulates in the deep gray matter [100, 101, 102] as they age and cognitive abilities generally decline with aging [108]. In addition, postmortem biochemical analyses of victims of neurodegenerative diseases such as Alzheimer's, Parkinson's, and Huntington's disease showed excessive iron levels at the basal ganglia region [109, 110, 111, 112, 113, 76]. Especially, there is evidence that iron deposits in the brain affect the cognitive ability of the aging population [114].

On the other hand, recent longitudinal exercise intervention studies of healthy older adults have shown that aerobic exercise, not stretching and toning, had positive effects on cognitive abilities [115, 116, 117, 118, 119]. Although many other factors such as diet play a role in the relationship between age and cognition, it would be interesting to see whether the changes of the (iron) patterns of the time-averaged T2* signals (which were already collected in those longitudinal studies) are different for the groups doing aerobic exercise vs. stretching and toning, and whether the positive effect of aerobic exercise is related to the amount or distribution of iron. Such findings would contribute to understanding the mechanisms underlying the benefits of aerobic exercise for cognitive abilities, in particular in relation to its effects on neuronal plasticity [115, 116, 117] and functional connectivity [119].

So far we have investigated a pre-defined region of interest (ROI) – the striatum – in a hypothesis-driven analysis, while many other brain regions such as the frontal and parietal lobes also play very important roles in learning new skills. Hence, it would be desirable to expand the analysis to an exploratory whole-brain analysis. Nevertheless, other regions outside these deep gray matter areas normally contain much less stored iron, and hence our learning prediction method based on stored iron patterns captured in time-averaged T2*-signal might not be successfully applicable. Yet even in that case, whole-brain analysis might help to confirm our hypothesis that iron is the underlying predictor of time-averaged T2*-signal and support the development and test of feature selection mechanisms of pattern analysis for brain MR data.

Among the regions that we have not examined, there is the hippocampus, of which iron content is high and changes with age [120]. Especially, studies on iron-deficiency, more notably during early development, have also demonstrated the effect of nonheme iron on hippocampus integrity [39, 40, 41]. As the hippocampus has a direct role in learning [121], patterns of brain nonheme iron captured in time-averaged T2* in the hippocampus might be particularly important to investigate.

Furthermore, for the T2/T2*/T2'-maps, quantitative measurements based on the mono-exponential assumption are prone to estimation error, because mono-exponential is a very rough model for signal decay at each voxel. This is especially true for T2*/T2' due to their sensitivity to field inhomogeneity, for example, caused by imperfect shimming. As a consequence it is usually preferable to have many echoes with many different TEs with a range corresponding to the range of T2/T2*/T2' values in the white/gray matter in the brain [70]. In any case, doing the measurement a few times and then averaging before fitting to the exponential models should yield more accurate results as a result of noise suppression.

Our hypothesis would be best tested by a sequence that can measure nonheme iron concentration in the brain more precisely and even directly. One non-invasive possibility is using the field-dependent-R2-increase (FDRI) which is shown to be more precise in measuring nonheme iron only [104, 122, 123]. But note that FDRI method requires two MR scanners at different field strengths.

5.2 Conclusions

From both 2008 and 2010 studies, we have consistently shown that the predictive information in time-averaged T2*-weighted images comes from the dorsal but not the ventral striatum. Furthermore, the prediction results from different MR measurements ranging from DTI over T2-weighted, T1-weighted maps to SWI, T2-map, T2*-map, and ASL have verified our hypothesis that successful learning prediction in time-averaged T2*-signal stems from paramagnetic nonheme-iron patterns. These patterns may be of ferritin as the molecule carries thousands of iron atoms that can affect the local field and hence MR signals at the macroscopic level. In normal BOLD acquisition, these signals are very weak and surpassed by other signals; they are strengthened sufficiently through taking the time average. The differences between individuals can be identified by the multi-voxel pattern analysis and using SVR predictor.

There are some differences in the prediction results between study 2010 and 2008. For example, time-averaged T2*-weighted signal in the caudate in study 2010 has lower prediction rate than in study 2008. This might be related to the fact that we used parallel imaging with GRAPPA mode (acceleration factor for phase encoding direction is 2) in study 2010 while in 2008 parallel acquisition was turned off.

Furthermore, recall that the iron-related information that helps predict learning might only reflect learners' abilities to improve, while how much one can learn in fact also depends on other factors such as learning approach or training strategies. In our two studies, participants were trained with different paradigms as well as in different durations of game play. In the 2008 study some subjects were instructed to follow fixed priority training, and some practiced with variable priority regime; all practiced for 20 hours. In 2010, participants were trained for only 10 hours, and all were given instructions of variable priority training. These differences could contribute to the overall performance of participants and might affect the prediction outcomes.

Last, that we used the gradient-echo EPI brain images, standard modality, to measure functional activity could make our new analysis technique especially

attractive, because no new scans would need to be added to established experimental protocols. In fact, the technique could be used to analyze existing data retrospectively.

REFERENCES

[1] P. L. Ackerman and A. T. Cianciolo, "Cognitive, perceptual-speed, and psychomotor determinants of individual differences during skill acquisition," *Journal of Experimental Psychology: Applied*, vol. 6, no. 4, pp. 259–90, 2000.

[2] P. L. Ackerman, R. Kanfer, and M. Goff., "Cognitive and noncognitive determinants and consequences of complex skill acquisition," *Journal of Experimental Psychology: Applied*, vol. 1, no. 4, pp. 270–304, 1995.

[3] M. Tufflash, R. Roring, and K. Ericsson, "Expert performance in SCRABBLE: implications for the study of the structure and acquisition of complex skills," *Journal of Experimental Psychology: Applied*, vol. 13, no. 3, pp. 124–134, 2007.

[4] K. I. Erickson, W. R. Boot, C. Basak, M. B. Neider, R. S. Prakash, M. W. Voss, A. N. Graybiel, D. J. Simons, M. Fabiani, G. Gratton, and A. F. Kramer, "Striatal volume predicts level of video game skill acquisition," *Cerebral Cortex*, vol. 20, no. 11, pp. 2522–2530, 2010.

[5] S. Ogawa, T. M. Lee, A. S. Nayak, and P. Glynn, "Oxygenation-sensitive contrast in magnetic resonance image of rodent brain at high magnetic fields," *Magnetic Resonance in Medicine*, vol. 14, no. 1, pp. 68–78, 1990.

[6] E. M. Haacke, Y. Xu, Y. N. Cheng, and J. R. Reichenbach, "Susceptibility weighted imaging (SWI)," *Magnetic Resonance in Medicine*, vol. 52, no. 3, pp. 612–618, Sep. 2004.

[7] M. E. Haacke, S. Mittal, Z. Wu, J. Neelavalli, and Y. N. Cheng, "Susceptibility-Weighted imaging: Technical aspects and clinical applications, part 1," *American Journal of Neuroradiology*, vol. 30, pp. 19–30, 2009.

[8] L. J. Anderson, S. Holden, B. Davis, E. Prescott, C. C. Charrier, N. H. Bunce, D. N. Firmin, B. Wonke, J. Porter, J. M. Walker, and D. J. Pennell, "Cardiovascular t2-star (T2*) magnetic resonance for the early diagnosis of myocardial iron overload," *European Heart Journal*, vol. 22, no. 23, pp. 2171–2179, Dec. 2001.

[9] S. Yehuda, M. E. Youdim, and D. I. Mostofsky, "Brain iron-deficiency causes reduced learning capacity in rats," *Pharmacology, Biochemistry, and Behavior*, vol. 25, no. 1, pp. 141–144, July 1986.

[10] A. B. Bruner, A. Joffe, A. K. Duggan, J. F. Casella, and J. Brandt, "Randomised study of cognitive effects of iron supplementation in non-anaemic iron-deficient adolescent girls," *Lancet*, vol. 348, no. 9033, pp. 992–996, Oct. 1996.

[11] S. J. B. Fretham, E. S. Carlson, and M. K. Georgieff, "The role of iron in learning and memory," *Advances in Nutrition: An International Review Journal*, vol. 2, no. 2, pp. 112 –121, Mar. 2011.

[12] C. S. Green and D. Bavelier, "Action video game modifies visual selective attention," *Nature*, vol. 423, no. 6939, pp. 534–537, May 2003.

[13] C. S. Green and D. Bavelier, "Enumeration versus multiple object tracking: the case of action video game players," *Cognition*, vol. 101, no. 1, pp. 217–245, Aug. 2006.

[14] D. Ansari, R. H. Grabner, K. Koschutnig, G. Reishofer, and F. Ebner, "Individual differences in mathematical competence modulate brain responses to arithmetic errors: An fMRI study," *Learning and Individual Differences*, vol. 21, no. 6, pp. 636–643, Dec. 2011.

[15] M. M. Gullick, L. A. Sprute, and E. Temple, "Individual differences in working memory, nonverbal IQ, and mathematics achievement and brain mechanisms associated with symbolic and nonsymbolic number processing," *Learning and Individual Differences*, vol. 21, no. 6, pp. 644–654, Dec. 2011.

[16] G. E. Alexander, M. R. DeLong, and P. L. Strick, "Parallel organization of functionally segregated circuits linking basal ganglia and cortex," *Annual Review of Neuroscience*, vol. 9, pp. 357–81, 1986.

[17] T. D. Barnes, Y. Kubota, D. Hu, D. Z. Jin, and A. M. Graybiel, "Activity of striatal neurons reflects dynamic encoding and recoding of procedural memories," *Nature*, vol. 437, no. 7062, pp. 1158–61, 2005.

[18] A. M. Graybiel, "The basal ganglia: learning new tricks and loving it," *Current Opinion in Neurobiology*, vol. 15, no. 6, pp. 638–44, 2005.

[19] A. M. Graybiel, "Habits, rituals, and the evaluative brain," *Annual Review of Neuroscience*, vol. 31, pp. 359–87, 2008.

[20] N. Meiran, G. Friedman, and E. Yehene, "Parkinson's disease is associated with goal setting deficits during task switching," *Brain and Cognition*, vol. 54, no. 3, pp. 260–2, 2004.

[21] M. Amalric and G. F. Koob, "Depletion of dopamine in the caudate nucleus but not in nucleus accumbens impairs Reaction-Time performance in rats," *The Journal of Neuroscience*, vol. 7, no. 7, pp. 2129–2134, 1987.

[22] D. Belin and B. J. Everitt, "Cocaine seeking habits depend upon dopamine-dependent serial connectivity linking the ventral with the dorsal striatum," *Neuron*, vol. 57, no. 3, pp. 432–41, 2008.

[23] B. De Martino, D. Kumaran, B. Holt, and R. J. Dolan, "The neurobiology of reference-dependent value computation," *Journal of Neuroscience*, vol. 29, no. 12, pp. 3833–42, 2009.

[24] H. E. Atallah, D. Lopez-Paniagua, J. W. Rudy, and R. C. O'Reilly, "Separate neural substrates for skill learning and performance in the ventral and dorsal striatum," *Nature Neuroscience*, vol. 10, no. 1, pp. 126–31, 2007.

[25] P. J. Hernandez, K. Sadeghian, and A. E. Kelley, "Early consolidation of instrumental learning requires protein synthesis in the nucleus accumbens," *Nature Neuroscience*, vol. 5, no. 12, pp. 1327–31, 2002.

[26] J. O'Doherty, P. Dayan, J. Schultz, R. Deichmann, K. Friston, and R. J. Dolan, "Dissociable roles of ventral and dorsal striatum in instrumental conditioning," *Science*, vol. 304, no. 5669, pp. 452–4, 2004.

[27] M. J. Koepp, R. N. Gunn, A. D. Lawrence, V. J. Cunningham, A. Dagher, T. Jones, D. J. Brooks, C. J. Bench, and P. M. Grasby, "Evidence for striatal dopamine release during a video game," *Nature*, vol. 393, no. 6682, pp. 266–8, 1998.

[28] T. W. Robbins and B. J. Everitt, "Functions of dopamine in the dorsal and ventral striatum," *Seminars in Neuroscience*, vol. 4, no. 2, pp. 119–127, Apr. 1992.

[29] W. Schultz, P. Apicella, and T. Ljungberg, "Responses of monkey dopamine neurons to reward and conditioned stimuli during successive steps of learning a delayed response task," *The Journal of Neuroscience*, vol. 13, no. 3, pp. 900–913, Mar. 1993.

[30] S. Sigala, C. Missale, and P. Spano, "Opposite effects of dopamine d2 and d3 receptors on learning and memory in the rat," *European Journal of Pharmacology*, vol. 336, no. 2-3, pp. 107–112, Oct. 1997.

[31] E. Dahlin, A. S. Neely, A. Larsson, L. Backman, and L. Nyberg, "Transfer of learning after updating training mediated by the striatum," *Science*, vol. 320, no. 5882, pp. 1510–2, 2008.

[32] E. Dahlin, L. Bäckman, A. S. Neely, and L. Nyberg, "Training of the executive component of working memory: subcortical areas mediate transfer effects," *Restorative Neurology and Neuroscience*, vol. 27, no. 5, pp. 405–419, 2009.

[33] J. L. Beard and J. R. Connor, "Iron status and neural functioning," *Annual Review of Nutrition*, vol. 23, pp. 41–58, 2003.

[34] S. Yehuda, S. Rabinovitz, R. Carasso, and D. Mostofsky, "The effects of brain iron deficiency on cognitive and behavioral aspects," in *Iron Deficiency and Overload*, ser. Nutrition and Health, S. Yehuda and D. I. Mostofsky, Eds. Humana Press, 2010, pp. 195–206.

[35] L. Bianco, E. Unger, and J. Beard, "Iron deficiency and neuropharmacology," in *Iron Deficiency and Overload*, ser. Nutrition and Health, S. Yehuda and D. I. Mostofsky, Eds. Humana Press, 2010, pp. 141–158.

[36] K. M. Erikson, B. C. Jones, and J. L. Beard, "Iron deficiency alters dopamine transporter functioning in rat striatum," *The Journal of Nutrition*, vol. 130, no. 11, pp. 2831–2837, Nov. 2000.

[37] C. Nelson, K. Erikson, D. J. Piñero, and J. L. Beard, "In vivo dopamine metabolism is altered in Iron-Deficient anemic rats," *The Journal of Nutrition*, vol. 127, no. 12, pp. 2282–2288, Dec. 1997.

[38] J. Beard, K. M. Erikson, and B. C. Jones, "Neonatal iron deficiency results in irreversible changes in dopamine function in rats," *The Journal of Nutrition*, vol. 133, no. 4, pp. 1174–1179, Apr. 2003.

[39] B. Lozoff and M. K. Georgieff, "Iron deficiency and brain development," *Seminars in Pediatric Neurology*, vol. 13, no. 3, pp. 158–165, Sep. 2006.

[40] R. Rao, M. de Ungria, D. Sullivan, P. Wu, J. D. Wobken, C. A. Nelson, and M. K. Georgieff, "Perinatal brain iron deficiency increases the vulnerability of rat hippocampus to hypoxic ischemic insult," *The Journal of Nutrition*, vol. 129, no. 1, pp. 199–206, Jan. 1999.

[41] A. T. Schmidt, K. J. Waldow, W. M. Grove, J. A. Salinas, and M. K. Georgieff, "Dissociating the long-term effects of fetal/neonatal iron deficiency on three types of learning in the rat," *Behavioral Neuroscience*, vol. 121, no. 3, pp. 475–482, June 2007.

[42] G. S. Yu, T. M. Steinkirchner, G. A. Rao, and E. C. Larkin, "Effect of prenatal iron deficiency on myelination in rat pups." *The American Journal of Pathology*, vol. 125, no. 3, pp. 620–624, Dec. 1986.

[43] E. Myasnikova, A. Samsonova, M. Samsonova, and J. Reinitz, "Support vector regression applied to the determination of the developmental age of a drosophila embryo from its segmentation gene expression patterns," *Bioinformatics*, vol. 18, no. Suppl 1, pp. S87–S95, July 2002.

[44] K. Masayuki, K. Yasuo, F. Sadao, and I. Hiroyuki, "Position control of ultrasonic motor using support vector regression," *Journal of the Japan Society for Precision Engineering (CD-ROM)*, vol. 72, no. 5, pp. 596–601, 2006.

[45] C. J. Burges, "A tutorial on support vector machines for pattern recognition," *Data Mining and Knowledge Discovery*, vol. 2, pp. 121–167, 1998.

[46] A. Smola and B. Scholkopf, "A tutorial on support vector regression," *Statistics and Computing*, vol. 14, pp. 199–222, 2004.

[47] L. T. K. Vo, D. B. Walther, A. F. Kramer, K. I. Erickson, W. R. Boot, M. W. Voss, R. S. Prakash, H. Lee, M. Fabiani, G. Gratton, D. J. Simons, B. P. Sutton, and M. Y. Wang, "Predicting individuals' learning success from patterns of Pre-Learning MRI activity," *PLoS ONE*, vol. 6, no. 1, p. e16093, Jan. 2011.

[48] Z. Liang and P. Lauterbur, *Principles of Magnetic Resonance Imaging: A Signal Processing Perspective*. Wiley-IEEE Press, Oct. 1999.

[49] E. Donchin, M. Fabiani, and A. F. Sanders, "The learning strategies program: An examination of the strategies in skill acquisition," *Amsterdam, the Netherlands: Elsevier*, 1989.

[50] A. M. Mané and E. Donchin, "The space fortress game," *Acta Psychologica*, vol. 71, pp. 17–22, 1989.

[51] W. Boot, C. Basak, K. Erickson, M. Neider, D. Simons, M. Fabiani, G. Gratton, M. Voss, R. Prakash, H. Lee, K. Low, and A. Kramer, "Transfer of skill engendered by complex task training under conditions of variable priority," *Acta Psychologica*, vol. 135, no. 3, pp. 349–57, 2010.

[52] K. J. Friston, S. Williams, R. Howard, R. S. Frackowiak, and R. Turner, "Movement-related effects in fMRI time-series," *Magnetic Resonance in Medicine: Official Journal of the Society of Magnetic Resonance in Medicine / Society of Magnetic Resonance in Medicine*, vol. 35, no. 3, pp. 346–355, Mar. 1996.

[53] M. Jenkinson, P. Bannister, M. Brady, and S. Smith, "Improved optimization for the robust and accurate linear registration and motion correction of brain images," *NeuroImage*, vol. 17, no. 2, pp. 825–841, Oct. 2002.

[54] J. Andersson, M. Jenkinson, and S. Smith, "Non-linear registration aka spatial normalisation," Department of Clinical Neurology, Oxford University, Oxford, UK., Technical Report TR07JA2, 2007.

[55] M. Jenkinson and S. Smith, "A global optimisation method for robust affine registration of brain images," *Medical Image Analysis*, vol. 5, no. 2, pp. 143–156, 2001.

[56] S. M. Smith, M. Jenkinson, M. W. Woolrich, C. F. Beckmann, T. E. Behrens, H. Johansen-Berg, P. R. Bannister, M. De Luca, I. Drobnjak, D. E. Flitney, R. K. Niazy, J. Saunders, J. Vickers, Y. Zhang, N. De Stefano, J. M. Brady, and P. M. Matthews, "Advances in functional and structural MR image analysis and

implementation as FSL," *NeuroImage*, vol. 23, no. Supplement 1, pp. S208–S219, 2004.

[57] S. Ogawa, T. M. Lee, A. R. Kay, and D. W. Tank, "Brain magnetic resonance imaging with contrast dependent on blood oxygenation." *Proceedings of the National Academy of Sciences of the United States of America*, vol. 87, no. 24, pp. 9868–9872, Dec. 1990.

[58] E. M. Haacke, N. Y. Cheng, M. J. House, Q. Liu, J. Neelavalli, R. J. Ogg, A. Khan, M. Ayaz, W. Kirsch, and A. Obenaus, "Imaging iron stores in the brain using magnetic resonance imaging," *Magnetic Resonance Imaging*, vol. 23, no. 1, pp. 1–25, Jan. 2005.

[59] Y. Zhang, M. Brady, and S. Smith, "Segmentation of brain MR images through a hidden Markov random field model and the expectation-maximization algorithm," *IEEE Transactions on Medical Imaging*, vol. 20, no. 1, pp. 45–57, Jan. 2001.

[60] J. Doyon, V. Penhune, and L. G. Ungerleider, "Distinct contribution of the cortico-striatal and cortico-cerebellar systems to motor skill learning," *Neuropsychologia*, vol. 41, no. 3, pp. 252–62, 2003.

[61] B. W. Balleine, M. Liljeholm, and S. B. Ostlund, "The integrative function of the basal ganglia in instrumental conditioning," *Behavioural Brain Research*, vol. 199, no. 1, pp. 43–52, 2009.

[62] H. H. Yin and B. J. Knowlton, "The role of the basal ganglia in habit formation," *Nature Reviews Neuroscience*, vol. 7, no. 6, pp. 464–76, 2006.

[63] M. E. Ragozzino, J. Jih, and A. Tzavos, "Involvement of the dorsomedial striatum in behavioral flexibility: role of muscarinic cholinergic receptors," *Brain Research*, vol. 953, no. 1-2, pp. 205–14, 2002.

[64] R. Cools, L. Clark, and T. W. Robbins, "Differential responses in human striatum and prefrontal cortex to changes in object and rule relevance," *The Journal of Neuroscience*, vol. 24, no. 5, pp. 1129–35, 2004.

[65] D. Gopher, M. Weil, and T. Bareket, "Transfer of skill from a computer game trainer to flight," *Human Factors*, vol. 36, pp. 387–405, 1994.

[66] C. Ouyang and B. P. Sutton, "Pseudo-continuous transfer insensitive labeling technique," *Magnetic Resonance in Medicine: Official Journal of the Society of Magnetic Resonance in Medicine / Society of Magnetic Resonance in Medicine*, vol. 66, no. 3, pp. 768–776, Sep. 2011.

[67] M. Brant-Zawadzki, G. D. Gillan, and W. R. Nitz, "MP RAGE: a three-dimensional, t1-weighted, gradient-echo sequence–initial experience in the brain," *Radiology*, vol. 182, no. 3, pp. 769 –775, Mar. 1992.

[68] M. P. Lichy, B. M. Wietek, J. P. I. Mugler, W. Horger, M. I. Menzel, A. Anastasiadis, K. Siegmann, T. Niemeyer, A. Königsrainer, B. Kiefer, F. Schick, C. D. Claussen, and H. Schlemmer, "Magnetic resonance imaging of the body trunk using a single-slab, 3-dimensional, t2-weighted turbo-spin-echo sequence with high sampling efficiency (SPACE) for high spatial resolution imaging: Initial clinical experiences," *Investigative Radiology*, vol. 40, no. 12, pp. 754 –760, 2005.

[69] S. J. Kirsch, R. W. Jacobs, L. L. Butcher, and J. Beatty, "Prolongation of magnetic resonance t2 time in hippocampus of human patients marks the presence and severity of Alzheimer's disease," *Neuroscience Letters*, vol. 134, no. 2, pp. 187–190, Jan. 1992.

[70] K. P. Whittall, A. L. MacKay, and D. K. B. Li, "Are mono-exponential fits to a few echoes sufficient to determine t2 relaxation for in vivo human brain?" *Magnetic Resonance in Medicine*, vol. 41, no. 6, pp. 1255–1257, June 1999.

[71] J. P. Wansapura, S. K. Holland, R. S. Dunn, and W. R. Ball, "NMR relaxation times in the human brain at 3.0 tesla," *Journal of Magnetic Resonance Imaging*, vol. 9, no. 4, pp. 531–538, 1999.

[72] K. P. Whittall, A. L. Mackay, D. A. Graeb, R. A. Nugent, D. K. Li, and D. W. Paty, "In vivo measurement of t2 distributions and water contents in normal human brain," *Magnetic Resonance in Medicine*, vol. 37, no. 1, pp. 34–43, 1997.

[73] J. Vymazal, R. A. Brooks, C. Baumgarner, V. Tran, D. Katz, J. W. Bulte, R. Bauminger, and G. Di Chiro, "The relation between brain iron and NMR relaxation times: an in vitro study," *Magnetic Resonance in Medicine: Official Journal of the Society of Magnetic Resonance in Medicine / Society of Magnetic Resonance in Medicine*, vol. 35, no. 1, pp. 56–61, Jan. 1996.

[74] J. F. Schenck, "The role of magnetic susceptibility in magnetic resonance imaging: MRI magnetic compatibility of the first and second kinds," *Medical Physics*, vol. 23, no. 6, pp. 815–850, June 1996.

[75] J. F. Schenck, "Magnetic resonance imaging of brain iron," *Journal of the Neurological Sciences*, vol. 207, pp. 99–102, Mar. 2003.

[76] S. D. Brass, N.-k. Chen, R. V. Mulkern, and R. Bakshi, "Magnetic resonance imaging of iron deposition in neurological disorders," *Topics in Magnetic Resonance Imaging*, vol. 17, no. 1, pp. 31–40, Feb. 2006.

[77] P. D. Griffiths, B. R. Dobson, G. R. Jones, and D. T. Clarke, "Iron in the basal ganglia in Parkinson's disease," *Brain*, vol. 122, no. 4, pp. 667–673, 1999.

[78] S. L. Harder, K. M. Hopp, H. Ward, H. Neglio, J. Gitlin, and D. Kido, "Mineralization of the deep gray matter with age: A retrospective review with susceptibility-weighted MR imaging," *American Journal of Neuroradiology*, vol. 29, no. 1, pp. 176–183, 2008.

[79] N. Raz, K. M. Rodrigue, and M. E. Haacke, "Brain aging and its modifiers: Insights from in vivo neuromorphometry and susceptibility weighted imaging," *Annals of the New York Academy of Sciences*, vol. 1097, pp. 84–93, 2007.

[80] J. Vymazal, M. Hajek, N. Patronas, J. N. Giedd, J. W. Bulte, C. Baumgarner, V. Tran, and R. A. Brooks, "The quantitative relation between t1-weighted and t2-weighted MRI of normal gray matter and iron concentration," *J Magn Reson Imaging*, vol. 5, no. 5, pp. 554–60, 1995.

[81] E. M. Haacke and J. R. Reichenbach, *Susceptibility Weighted Imaging in MRI: Basic Concepts and Clinical Applications*, 1st ed. Wiley-Blackwell, Feb. 2011.

[82] Y. Wang, Y. Yu, D. Li, K. T. Bae, J. J. Brown, W. Lin, and E. M. Haacke, "Artery and vein separation using susceptibility-dependent phase in contrast-enhanced MRA," *Journal of Magnetic Resonance Imaging*, vol. 12, no. 5, pp. 661–670, Nov. 2000.

[83] E. M. Haacke, M. Ayaz, A. Khan, E. S. Manova, B. Krishnamurthy, L. Gollapalli, C. Ciulla, I. Kim, F. Petersen, and W. Kirsch, "Establishing a baseline phase behavior in magnetic resonance imaging to determine normal vs. abnormal iron content in the brain," *Journal of Magnetic Resonance Imaging*, vol. 26, no. 2, pp. 256–264, Aug. 2007.

[84] B. Hallgren and P. Sourander, "The effect of age on the non-haemin iron in the human brain," *Journal of Neurochemistry*, vol. 3, no. 1, pp. 41–51, Oct. 1958.

[85] T. Riggins, N. C. Miller, P. J. Bauer, M. K. Georgieff, and C. A. Nelson, "Consequences of low neonatal iron status due to maternal diabetes mellitus on explicit memory performance in childhood," *Developmental Neuropsychology*, vol. 34, no. 6, pp. 762–779, 2009.

[86] S. Yehuda and M. Yehuda, "Long lasting effects of infancy iron deficiency–preliminary results," *Journal of Neural Transmission. Supplementum*, no. 71, pp. 197–200, 2006.

[87] M. B. H. Youdim, A. R. Green, M. B. H. Youdim, and A. R. Green, "Biogenic monoamine metabolism and functional activity in IronâĂŘDeficient rats: Behavioural correlates," in *Ciba Foundation Symposium 51 âĂŘ Iron Metabolism*. John Wiley & Sons, Ltd., 1977, pp. 201–225.

[88] J. F. Schenck, "Imaging of brain iron by magnetic resonance: T2 relaxation at different field strengths," *Journal of the Neurological Sciences*, vol. 134, Supplement, no. 0, pp. 10–18, Dec. 1995.

[89] P. J. Basser, J. Mattiello, and D. LeBihan, "MR diffusion tensor spectroscopy and imaging," *Biophysical Journal*, vol. 66, no. 1, pp. 259–267, Jan. 1994.

[90] P. Basser and C. Pierpaoli, "Microstructural and physiological features of tissues elucidated by quantitative-diffusion-tensor MRI," *Journal of Magnetic Resonance - Series B*, vol. 111, no. 3, pp. 209–219, 1996.

[91] D. L. Bihan, J. Mangin, C. Poupon, C. A. Clark, S. Pappata, N. Molko, and H. Chabriat, "Diffusion tensor imaging: Concepts and applications," *Journal of Magnetic Resonance Imaging*, vol. 13, no. 4, pp. 534–546, 2001.

[92] C. Pierpaoli and P. J. Basser, "Toward a quantitative assessment of diffusion anisotropy," *Magnetic Resonance in Medicine*, vol. 36, no. 6, pp. 893–906, Dec. 1996.

[93] E. C. Wong, R. B. Buxton, and L. R. Frank, "A theoretical and experimental comparison of continuous and pulsed arterial spin labeling techniques for quantitative perfusion imaging," *Magnetic Resonance in Medicine*, vol. 40, no. 3, pp. 348–355, Sep. 1998.

[94] E. P. Gilissen, R. E. Jacobs, and J. M. Allman, "Magnetic resonance microscopy of iron in the basal forebrain cholinergic structures of the aged mouse lemur," *Journal of the Neurological Sciences*, vol. 168, no. 1, pp. 21–27, Sep. 1999.

[95] J. R. Reichenbach, R. Venkatesan, D. A. Yablonskiy, M. R. Thompson, S. Lai, and E. M. Haacke, "Theory and application of static field inhomogeneity effects in gradient-echo imaging," *Journal of Magnetic Resonance Imaging*, vol. 7, no. 2, pp. 266–279, Mar. 1997.

[96] Y. Gossuin, R. N. Muller, and P. Gillis, "Relaxation induced by ferritin: a better understanding for an improved MRI iron quantification," *NMR in Biomedicine*, vol. 17, no. 7, pp. 427–432, Nov. 2004.

[97] C. Schenker, D. Meier, W. Wichmann, P. Boesiger, and A. Valavanis, "Age distribution and iron dependency of the t2 relaxation time in the globus pallidus and putamen," *Neuroradiology*, vol. 35, no. 2, pp. 119–124, 1993.

[98] R. J. Ordidge, J. M. Gorell, J. C. Deniau, R. A. Knight, and J. A. Helpern, "Assessment of relative brain iron concentrations usingT2-weighted andT2*-weighted MRI at 3 tesla," *Magnetic Resonance in Medicine*, vol. 32, no. 3, pp. 335–341, Sep. 1994.

[99] M. A. Griswold, P. M. Jakob, Q. Chen, J. W. Goldfarb, W. J. Manning, R. R. Edelman, and D. K. Sodickson, "Resolution enhancement in single-shot imaging using simultaneous acquisition of spatial harmonics (SMASH)," *Magnetic Resonance in Medicine*, vol. 41, no. 6, pp. 1236–1245, June 1999.

[100] J. Pujol, C. Junque, P. Vendrell, J. Grau, J. Marti-Vilalta, C. Olive, and J. Gili, "Biological significance of iron-related magnetic resonance imaging changes in the brain," *Archives of Neurology*, vol. 49, no. 7, pp. 711–717, 1992.

[101] G. Bartzokis, J. Mintz, D. Sultzer, P. Marx, J. Herzberg, C. Phelan, and S. Marder, "In vivo MR evaluation of age-related increases in brain iron," *American Journal of Neuroradiology*, vol. 15, no. 6, pp. 1129–1138, 1994.

[102] G. Bartzokis, T. Tishler, P. Lu, P. Villablanca, L. Altshuler, M. Carter, D. Huang, N. Edwards, and J. Mintz, "Brain ferritin iron may influence age- and gender-related risks of neurodegeneration," *Neurobiology of Aging*, vol. 28, no. 3, pp. 414–423, 2007.

[103] A. Pfefferbaum, E. Adalsteinsson, T. Rohlfing, and E. V. Sullivan, "Diffusion tensor imaging of deep gray matter brain structures: Effects of age and iron concentration," *Neurobiology of Aging*, vol. 31, no. 3, pp. 482–493, Mar. 2010.

[104] G. Bartzokis, M. Aravagiri, W. H. Oldendorf, J. Mintz, and S. R. Marder, "Field dependent transverse relaxation rate increase may be a specific measure of tissue iron stores," *Magnetic Resonance in Medicine*, vol. 29, no. 4, pp. 459–464, Apr. 1993.

[105] R. M. Torack, H. Alcala, M. Gado, and R. Burton, "Correlative assay of computerized cranial tomography CCT, water content and specific gravity in normal and pathological postmortem brain," *Journal of Neuropathology and Experimental Neurology*, vol. 35, no. 4, pp. 385–392, July 1976.

[106] P. P. Michel, S. Vyas, and Y. Agid, "Toxic effects of iron for cultured mesencephalic dopaminergic neurons derived from rat embryonic brains," *Journal of Neurochemistry*, vol. 59, no. 1, pp. 118–127, July 1992.

[107] J. Lan and D. H. Jiang, "Excessive iron accumulation in the brain: A possible potential risk of neurodegeneration in Parkinson's disease," *Journal of Neural Transmission*, vol. 104, pp. 649–660, June 1997.

[108] T. A. Salthouse, "Selective review of cognitive aging," *Journal of the International Neuropsychological Society*, vol. 16, no. 05, pp. 754–760, 2010.

[109] J. E. Nielsen, L. N. Jensen, and K. Krabbe, "Hereditary haemochromatosis: a case of iron accumulation in the basal ganglia associated with a Parkinsonian syndrome." *Journal of Neurology, Neurosurgery & Psychiatry*, vol. 59, no. 3, pp. 318 –321, 1995.

[110] P. Riederer, E. Sofic, W. D. Rausch, B. Schmidt, G. P. Reynolds, K. Jellinger, and M. B. Youdim, "Transition metals, ferritin, glutathione, and ascorbic acid in Parkinsonian brains," *Journal of Neurochemistry*, vol. 52, no. 2, pp. 515–520, Feb. 1989.

[111] D. Loeffler, J. Connor, P. Juneau, B. Snyder, L. Kanaley, A. DeMaggio, H. Nguyen, C. Brickman, and P. LeWitt, "Transferrin and iron in normal, Alzheimer's disease, and Parkinson's disease brain regions," *Journal of Neurochemistry*, vol. 65, no. 2, pp. 710–716, 1995.

[112] G. Bartzokis and T. Tishler, "MRI evaluation of basal ganglia ferritin iron and neurotoxicity in Alzheimer's and Huntingon's disease." *Cellular and Molecular Biology*, vol. 46, no. 4, pp. 821–833, 2000.

[113] J. Chen, P. Hardy, W. Kucharczyk, M. Clauberg, J. Joshi, A. Vourlas, M. Dhar, and R. Henkelman, "MR of human postmortem brain tissue: Correlative study between t2 and assays of iron and ferritin in Parkinson and Huntington disease," *American Journal of Neuroradiology*, vol. 14, no. 2, pp. 275–281, 1993.

[114] L. Penke, M. C. Valdés Hernandéz, S. M. Maniega, A. J. Gow, C. Murray, J. M. Starr, M. E. Bastin, I. J. Deary, and J. M. Wardlaw, "Brain iron deposits are associated with general cognitive ability and cognitive aging," *Neurobiology of Aging*, vol. 33, no. 3, pp. 510–517.e2, Mar. 2012.

[115] S. J. Colcombe, K. Erickson, P. Scalf, J. Kim, R. Prakash, E. McAuley, S. Elavsky, D. Marquez, L. Hu, and A. Kramer, "Aerobic exercise training increases brain volume in aging humans," *Journal of Gerontology: Medical Sciences*, vol. 61, pp. 1166–1170, 2006.

[116] S. J. Colcombe, A. Kramer, K. Erickson, P. Scalf, E. McAuley, N. Cohen, A. Webb, G. Jerome, D. Marquez, and S. Elavsky, "Cardiovascular fitness, cortical plasticity, and aging," *Proceedings of the National Academy of Sciences USA*, vol. 101, no. 9, pp. 3316–3321, 2004.

[117] K. I. Erickson, R. S. Prakash, M. W. Voss, L. Chaddock, L. Hu, K. Morris, S. White, T. Wojcicki, E. McAuley, and A. F. Kramer, "Aerobic fitness is associated with hippocampal volume in elderly humans," *Hippocampus*, vol. 19, no. 10, pp. 1030–1039, 2009.

[118] A. F. Kramer, S. Hahn, N. Cohen, M. Banich, E. McAuley, C. Harrison, J. Chason, E. Vakil, L. Bardell, R. Boileau, and A. Colcombe, "Aging, fitness, and neurocognitive function," *Nature*, vol. 400, pp. 418–419, 1999.

[119] M. W. Voss, R. Prakash, K. Erickson, C. Basak, J. Kim, S. Heo, A. Szabo, S. White, T. Wojcicki, E. Mailey, N. Gothe, E. McAuley, and A. Kramer, "Plasticity of brain networks in a randomized intervention trial of exercise training in older adults," *Frontiers in Aging Neuroscience*, vol. 2, 2010.

[120] J. Savory, J. K. Rao, Y. Huang, P. R. Letada, and M. M. Herman, "Age-related hippocampal changes in Bcl-2:Bax ratio, oxidative stress, redox-active iron and apoptosis associated with aluminum-induced neurodegeneration: increased susceptibility with aging," *Neurotoxicology*, vol. 20, no. 5, pp. 805–817, Oct. 1999.

[121] L. E. Jarrard, "On the role of the hippocampus in learning and memory in the rat," *Behavioral & Neural Biology*, vol. 60, no. 1, pp. 9–26, 1993.

[122] G. Bartzokis, D. Sultzer, J. Cummings, L. E. Holt, D. B. Hance, V. W. Henderson, and J. Mintz, "In vivo evaluation of brain iron in Alzheimer disease using magnetic resonance imaging," *Archives of General Psychiatry*, vol. 57, no. 1, pp. 47–53, Jan. 2000.

[123] A. Pfefferbaum, E. Adalsteinsson, T. Rohlfing, and E. V. Sullivan, "MRI estimates of brain iron concentration in normal aging: Comparison of field-dependent (FDRI) and phase (SWI) methods," *NeuroImage*, vol. 47, no. 2, pp. 493–500, Aug. 2009.